博士學位論文

A Sub-domain based Regularization Method in Electrical Impedance Tomography

濟州大學校 大學院

에너지應用시스템學部 電子工學專攻

姜 淑 仁

2017年 2月

전기 임피던스 단층촬영법에서 부분영역 기반 조정기법

指導敎授 金 慶 淵

姜 淑 仁

이 論文을 工學 博士學位 論文으로 提出함

2016年 12月

姜淑仁의 工學 博士學位 論文을 認准함

審査委員長 _____ (印)

委　　員 _____ (印)

委　　員 _____ (印)

委　　員 _____ (印)

委　　員 _____ (印)

濟州大學校 大學院

2016年 12月

A Sub-domain based Regularization Method in Electrical Impedance Tomography

Suk In Kang

(Supervised by Professor Kyung-Youn Kim)

A thesis submitted in partial fulfillment of the requirement for the degree of Doctor of Philosophy in Electrionic Engineering.

2016. 12

The thesis has been examined and approved.

Thesis director, Min-Jae Kang, Professor, Department of Electronic Engineering
JEJU NATIONAL UNIVERSITY

In-Soo Lee, Professor, School of Electronics Engineering
KYUNGPOOK NATIONAL UNIVERSITY

Sung-Taek Ko, Professor, Department of Electronic Engineering
JEJU NATIONAL UNIVERSITY

Seokjun Ko, Associate Professor, Department of Electronic Engineering
JEJU NATIONAL UNIVERSITY

Kyung-Youn Kim, Professor, Department of Electronic Engineering
JEJU NATIONAL UNIVERSITY

2016.12
Date

Faculty of Applied Energy System, Major of Electronic Engineering

GRADUATE SCHOOL

JEJU NATIONAL UNIVERSITY

Contents

Abbreviations and Notations

BEM	Boundary element method
CC	Correlation coefficient
CEM	Complete electrode model
CRM	Conventional regularization method
CT	Computer tomography
EIT	Electrical impedance tomography
FDM	Finite difference method
FEM	Finite element method
ICU	Intensive care unit
IE	Image error
LS	Least squares
MRI	Magnetic resonance imaging
PRM	Proposed regularization method
TV	Total variation
Ω	Computational domain of object
A	Magnetic potential, Class in Otsu's thresholding method
B	Magnetic flux density, Class in Otsu's thresholding method
D	Electric flux density
E	Electric field
H	Magnetic field, Jacobian
u	Electric potential
J	Current density
J_o	Ohmic current
J_s	Current source
ε	Permittivity
μ	Permeability
σ	Conductivity
ρ	Resistivity

ω	Frequency
v	Volume
S	Surface of v
$\mathbf{n}$	Unit normal vector
j_n	Negative normal component of the injected density J_s
L	Number of electrodes
z_l	Contact impedance of lth electrode
e_l	lth electrode
U_l	Voltage on lth electrode
$\tilde{U}$	Measured voltage
I_l	Injected current to the lth electrode
N_n, N_e, N_l	Number of FEM nodes, elements, and edges, respectively
N_m	Number of voltage data
u^h	Finite element approximation of the electric potential u
U^h	Finite element approximation of the voltages on the electrodes
ϕ_i	Basis function for i th node in FEM
$\mathbf{m}_j$	Arbitrary vector ensuring Kirchhoff's voltage law
α_i, β_j	Coefficient to be determined using FEM
w	Arbitrary weighting function for the basis function ϕ_i
W_l	Arbitrary weighting function for lth electrode of $\mathbf{m}_j$
$\mathbf{A}$	Stiffness matrix in FEM
$\mathbf{b}$	Unknowns to be solved in FEM
$\mathbf{B}$, $\mathbf{C}$, $\mathbf{D}$	Component of stiffness matrix $\mathbf{A}$
I	Current pattern
$\mathbf{I}$	Identity matrix
ξ_m, ξ_r	Measurement error, residual error, respectively
$\hat{\rho}$	Estimated resistivity distribution
$\bar{\rho}$	Mean values of the true resistivity distribution ρ

$\bar{\hat{\rho}}$	Mean values of the estimated resistivity distribution $\hat{\rho}$
ρ_c	Estimated current distribution
ρ_*	*Prior* estimate of ρ
ρ_h	Best homogenous resistivity distribution
Γ	Regularization matrix
Γ_k	k th row of regularization matrix
Γ^*	New difference matrix of Γ
γ	Regularization parameter
ς	Regularization parameter in the sub-domain based regularization method
$\mathbf{L}$	Regularization matrix in total variation regularization method
$\mathbf{L}_k$	k th row of total variation operator $\mathbf{L}$
λ	Singular value
$\chi_k(x,y)$	Characteristic function of the k th FEM element
D_ρ	Diagonal matrix used in $l1$-norm regularization method
D_{TV}	Diagonal matrix used in total regularization method
δ	Small positive value
T	Number of gray levels
o_j	Number of elements at level j
p	Probability distribution
t^*	Optimal threshold value using Otsu's thresholding method
ω_A, ω_B	Probability of each class occurrence
μ_A, μ_B	Each class mean
μ_T	Total mean level
σ_A^2, σ_B^2	Each class variance
σ_T^2	Total variation of levels
σ_{within}^2, $\sigma_{between}^2$	Within-class variance, between-class variance, respectively

List of Figures

List of Tables

초 록

전기 임피던스 단층촬영법(electrical impedance tomography; EIT)은 MRI 나 CT 등과 같은 단층촬영법의 일종이다. EIT 는 물체 표면에 부착된 전극에 전류를 주입하고 유기된 전압을 측정하여 영상 복원 알고리즘으로 물체 내부의 미지 저항률 분포를 추정하고 이를 영상화하는 기술이다.

EIT 에서의 영상복원은 일반적으로 계산전압과 측정전압의 차인 잔류오차의 최소자승문제로 다루어진다. 전압과 내부 저항률 분포와의 관계는 비선형이며, 주로 빠른 수렴성과 추정 정확도면에서 성능이 우수한 Gauss-Newton 알고리즘에 의해 내부 저항률 분포를 추정한다. 그러나, 이 경우의 영상복원은 이산적 비정치 문제(discrete ill-posed problem)의 일종으로 대부분의 경우에 있어 내부 저항률 분포 영상을 얻기가 어렵다. 그러므로, EIT 에서는 역문제의 비정치성을 완화하여 실제의 내부 저항률 분포에 대한 정보를 제공할 수 있는 의미있는 영상을 얻기 위해 최소자승문제의 부가적인 제약조건으로서 조정기법을 사용된다.

EIT 에서는 역문제 계산 시 difference 타입의 조정행렬을 갖는 일반화된 Tikhonov 조정기법을 주로 사용하는데, 이는 one-step 알고리즘에 적용할 수 있어 계산소모가 적고, 안정적으로 수렴성이 확보되는 장점을 갖고 있다. 그러나, 이 방법은 내부 저항률 분포의 갑작스런 변화를 제약하는 smoothness 가정을 전제로 하고 있어 복원된 영상에서 표적의 경계가 모호해지는 한계가 있다.

따라서, 본 논문에서는 표적의 경계를 뚜렷하게 나타내어 공간해상도를 향상시킬 수 있는 부분영역 기반 조정기법(sub-domain based regularization method)을 제안하였다. 제안한 조정기법에서는 물체 내부 구조에 대한 부분적인 정보가 알려져 있거나 가정할 수 있을 때 이를 부분영역(sub-domain)으로 간주하고 이에 대한 사전정보를 조정기법에 포함한다. 이를 위해 기존 등방성의 difference 타입 조정행렬을 비등방성으로 수정하고 부분영역마다 다른 조정 파라미터의 값을 사용한다. 그렇게 함으로써 부분영역 내의 저항률 변화는 부분영역 내에서만 영향을 끼치도록 하고 그 외 영역의 저항률 변화는 전체 영역에서 인접한 지역의 저항률 변화와 상호 영향을 미치도록 하였다. 제안한 기법은 인체 흉부 및 이상 유동장 모니터링에 적용하였으며, 복원 성능을 비교 분석하였다. 결과적으로 가공 데이터와 실험 데이터에 대한 영상복원 결과, 제안한 기법은 기존 방법에

비하여 타겟의 경계를 뚜렷하게 복원하고 부분영역에서는 균일한 분포를 나타냄으로써 개선된 영상을 얻을 수 있음을 보였다.

1. Introduction

Electrical impedance tomography (EIT) is a non-invasive imaging technique that estimates and reconstructs the internal resistivity distribution of the object. This technique is based on the fact that the organs or targets inside domain have different electrical resistivity. In fact, the quantity to be imaged in EIT is the impedivity, but since EIT often assumes that the resistive part of the impedivity dominates, it estimates the resistivity distribution.

EIT has been developed as an alternative to the medical imaging techniques such as computer tomography (CT), magnetic resonance imaging (MRI), ultrasonic imaging that are expensive and/or even cause adverse health effects. EIT has been applied for industrial and geophysical imaging in addition to medical imaging. EIT has been applied to several medical applications that include lung imaging (Brown 2001, Mueller *et al*. 2001), head imaging (Holder 1992), and breast imaging (Osterman *et al*. 2000, Cherepenin *et al*. 2002, Kerner *et al*. 2002). In industrial applications, EIT has been used to monitor flow processes such as two or multi-phase mixing in pipes (Jones *et al*. 1993, Dickin and Wang 1996, Pinheiro *et al*. 1997, George *et al.* 2000). In geophysics applications, resistivity imaging is widely used in exploring mineral resources, detection of faults, fractures, contaminant plumes, waste dumps, and geotechnical and environmental applications (Daily *et al*. 1992, Reynolds and Taylor 1996, Maillol *et al*. 1999, Casas *et al*. 2008). EIT is made up of relatively inexpensive hardware, and it contains fast data acquisition system thus has high temporal resolution characteristics. In addition, EIT system is portable and contains no health hazard due to its exposure to humans (Webster 1990, Williams and Beck 1995, Cheney *et al.* 1999). In medical applications, with the above advantages that EIT poses it can be used as a long-term bedside monitoring tool for diagnosis of patients in the intensive care unit (ICU). Also, in the industrial applications undergoing fast transient process, EIT can be used to visualize heterogeneous phase in the flow process because of its high temporal resolution. However, the reconstructed EIT images suffer from the poor spatial resolution compared to other image techniques due to diffusive characteristics of injected source energy and ill-posed nature of the inverse problem. Thus, the resolution of

reconstructed EIT images need to be improved to yield useful information from the measured voltage data.

In EIT, electrical current is injected through the electrodes attached to the surface of the object that is to be imaged, and the resulting excited voltages are measured on the electrode. Based on the current-voltage relationship, the resistivity distribution inside the object is reconstructed by using an image reconstruction algorithm. Schematic diagram of the EIT is shown in figure 1.1.

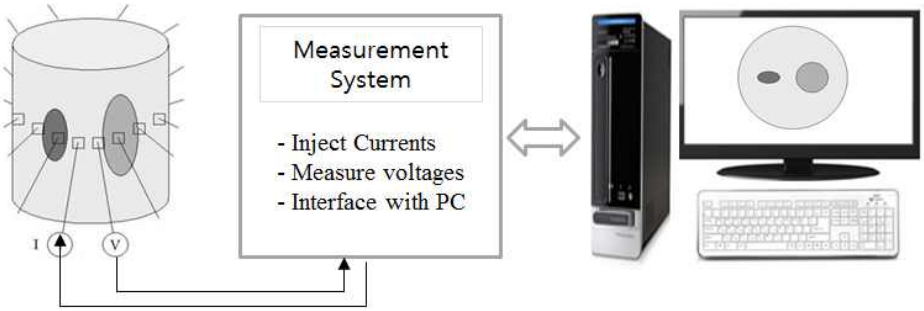

Figure 1.1. Schematic diagram illustrating the principle of EIT

Image reconstruction problem in EIT is to recover an unknown internal resistivity distribution from the measured voltages on the electrode, and it is usually treated as a least squares problem. That is, the resistivity distribution is estimated such that it minimizes the *l*2-norm of the difference between the measured voltages and calculated voltages. The reconstruction procedure is accomplished by solving the forward and inverse problem.

In the forward problem, with the assumed resistivity distribution inside the domain and the injected currents, the boundary voltages on the electrode are calculated by using a proper physical model. The physical model between the injected currents and the boundary voltages on the electrode is governed by a partial differential equation with boundary conditions. The analytical solution of forward problem is only possible for simple geometries (Choi *et al*. 2004, Kim *et al*. 2007). Therefore, for complex geometry, numerical methods are used instead of the analytical solution such as finite element method (Vauhkonen 1997, Jain *et al*. 1997, Polydorides and Lionheart 2002), boundary element method (de Munck *et al*. 2000, Cartwright *et al*. 2001, Khampampati *et al*. 2012).

In the inverse problem, with the measured voltage and injected current, the internal resistivity distribution is estimated by using Gauss-Newton algorithm as a common approach. The inverse problem in EIT is mathematically discrete ill-posed problem, thus it has a numerically unstable solution. That is, a small change in voltage measurement results in a large change in resistivity distribution. Therefore, in order to solve an ill-posed problem, the regularization method has to be used in reconstruction procedure. That is, the inversion process is imposed with an additional constraint using *a priori* knowledge of the true solution. Since the reconstruction resolution appears significantly different depending on the regularization method, the proper regularization method with regularization matrix and parameter should be used in the image reconstruction.

Commonly, the *l*2-norm regularization method known as a quadratic regularization method is used in EIT to penalize sudden variations in the resistivity. As a regularization matrix, the identity matrix (Yorkey *et al*. 1987), a positive diagonal matrix (Cheney *et al*. 1990), approximations of first and second order differential operator (Hua *et al*. 1988), and the inverse of a Gaussian matrix (Adler and Guardo 1996) can be mostly used. The *l*2-norm regularization method achieves stability of the inverse problem with rapid convergence. However, it is difficult to describe discrete variations in the reconstructed image that cannot differentiate the distinct variation in resistivity due to the smoothness assumption (Borsic *et al*. 2002). In addition, the resistivity of targets with high value is often underestimated, and the undesirable spots that can be regarded as targets are shown in the background region of the reconstructed image.

In order to have a better spatial resolution by preserving sharp transition between the target and background, there are several methods such as the total variation (TV) regularization method, the *l*1-norm regularization method, and the approach using the *prior* information of known internal structure. The TV regularization method (Dobson and Santosa 1994, Chung *et al*. 2005, Borsic *et al.* 2007) uses the total variation function in a regularization method and the constraint assumes the total variations in resistivity distribution are zero. The TV regularization method preserves discontinuities in the reconstructed images, but its performance is degraded by noise (Chan *et al*. 2005). The *l*1-norm regularization method is referred to as sparsity

regularization and its penalty function uses the *l*1-norm instead of the *l*2-norm. This method recently has been investigated intensively, and it can be successfully used in situations where small targets are located to close to each other (Jin *et al.* 2011, Gehre *et al.* 2012). The third approach is that of using the *prior* information of known internal structure by incorporating into the reconstruction procedure (Vauhkonen *et al.* 1998, Kaipio *et al.* 1999, Heikkinen *et al.* 2001, Kim *et al.* 2002a). This method can reconstruct sharp boundaries of targets and have a better resolution when the *prior* information is known with good accuracy.

The purpose of this thesis is to improve the spatial resolution in EIT images using a new regularization method. A new regularization method called a sub-domain based regularization method (Kang *et al.* 2016a, Kang *et al*. 2016b) developed in this thesis is inspired by the fact that a *prior* information on the internal structure of the object can improve the spatial resolution by being incorporated into the regularization method. Especially, this work is motivated from the *l*2-norm regularization method with the new difference-type regularization matrix modified by *prior* information (Heikkinen *et al.* 2001, Kim *et al.* 2002a). However, for most real situations, the *prior* information on the internal structure of the whole domain cannot be known exactly. If the *prior* information on internal structure is not reliable with an actual model, the reconstruction performance gets deteriorated.

Therefore, in this thesis, when the partial information on the internal structure is known or available, a sub-domain based regularization method is proposed to improve the spatial resolution in EIT. In the proposed sub-domain based regularization method, the modified difference regularization matrix is selected in a similar way to the previous method using the *prior* information on the known internal structure (Heikkinen *et al.* 2001, Kim *et al.* 2002a). However, the regularization matrix in the proposed sub-domain based regularization method is different from the previous methods that consider the known internal structure from the whole domain as to be separate. In the proposed method, the regularization matrix is constructed to consider the partially known internal structure as sub-domains. Also, the regularization parameter is set with different weight for the sub-domains. By doing so, the resistivity changes in the sub-domains have an effect on the resistivity changes within each sub-domain, however, the resistivity changes in

the regions excluding sub-domains are affected by the resistivity changes in whole domain. To investigate the performance of the proposed regularization method, two applications for human thorax monitoring and two-phase flow monitoring are considered. For the human thorax monitoring, available CT image is used to determine the sub-domains and the one-step Gauss-Newton algorithm is used as the reconstruction algorithm. For the two-phase flow monitoring, the part of background selected by using Otsu's thresholding method (Otsu 1979) after 1st iteration of Gauss-Newton algorithm is considered as a sub-domain and the iterative Gauss-Newton algorithm is used as the reconstruction algorithm.

This thesis contains five chapters. Chapter 1 gives an introduction as an overview of this thesis. Chapter 2 presents the image reconstruction in EIT using FEM and Gauss-Newton algorithm. In chapter 3, the common three regularization methods in EIT are presented. The proposed sub-domain based regularization method is presented in chapter 4. Finally, the conclusions of the thesis are given in chapter 5.

2. Image Reconstruction in EIT

Image reconstruction in EIT can be obtained by solving the forward problem and inverse problem. The forward problem is to calculate a unique result of a given cause by using a relative physical model. In EIT, the voltages as the solution of forward problem are calculated on the boundary electrodes with the given current injection and internal resistivity distribution. Conversely, the inverse problem is to seek the cause of a measured or given result. That is, in EIT, the internal resistivity distribution is estimated and reconstructed using the measured voltages and injected currents on the boundary electrodes. The principle of image reconstruction in EIT is shown in below figure 2.1.

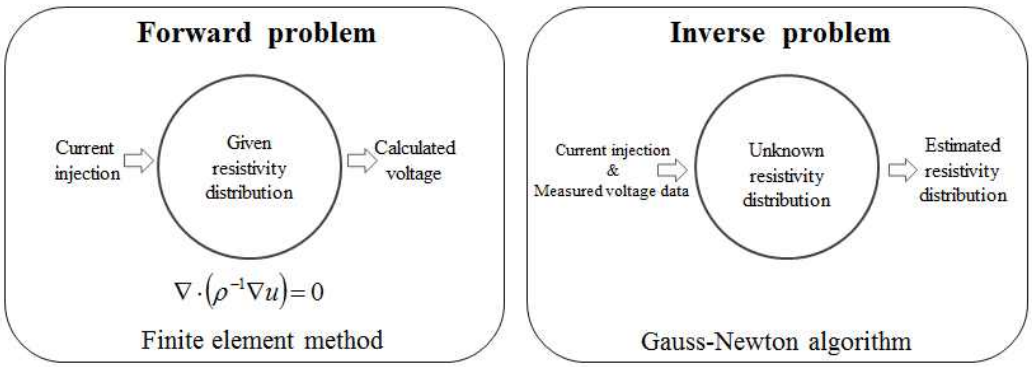

Figure 2.1. Forward problem vs. inverse problem in EIT

In order to estimate the resistivity distribution in EIT inverse problem, the forward solution for the physical model is needed. The physical model for the forward problem is governed by a partial differential equation with boundary conditions. Generally, it is difficult to formulate an analytical forward solution for a complex domain. Hence, to solve the forward problem, numerical methods are used such as finite element method (FEM), boundary element method (BEM) and finite difference method (FDM). In this thesis, FEM is used to solve the forward problem for two-dimensional (2D) computational domain. The inverse problem in EIT is usually treated as a least squares problem and several reconstruction algorithms are implemented. Among the reconstruction algorithms, Gauss-Newton algorithm is widely used method to estimate the resistivity distribution in EIT because of its rapid convergence and an estimated accuracy.

In section 2.1, the governing equation for EIT is derived through Maxwell equations, and boundary conditions and FEM formulation to solve the forward problem are presented. In addition, current injection methods for the data collection are introduced. In section 2.2, Gauss-Newton algorithm is reviewed as an inverse solver and the computation of Jacobian is derived for linearization to find the inverse solution.

2.1 Forward problem

2.1.1 Derivation of governing equation

The governing equation of the physical model can be derived through Maxwell equations (Barber and Brown 1984, Isaacson and Cheney, 1990, Vauhkonen 1997, Holder 2005).

The electromagnetic field in the two-dimensional domain Ω can be described as

$$\nabla \times E = -\frac{\partial B}{\partial t}, \tag{2.1}$$

$$\nabla \times H = J + \frac{\partial D}{\partial t}, \tag{2.2}$$

where E is the electric field, H is the magnetic field, D is the electric flux density, B is the magnetic flux density, and J is the current density. Here, the total current density J consists of ohmic current (J_o) and current source (J_s).

The electric field E can be expressed as

$$E = -\nabla u - \frac{\partial A}{\partial t}, \tag{2.3}$$

where u is electric potential and A is magnetic potential.

In a linear isotropic medium, the following relationships are valid

$$D = \varepsilon E, \tag{2.4}$$

$$B = \mu H, \tag{2.5}$$

$$J_o = \sigma E, \tag{2.6}$$

where ε, μ, and σ are permittivity, permeability, and conductivity of the medium, respectively.

If the injected currents are time harmonic with frequency ω, the electric field E and magnetic field H are

$$E = \tilde{E}e^{i\omega t}, \tag{2.7}$$

$$B = \tilde{B}e^{i\omega t}. \tag{2.8}$$

Substituting the equations (2.4) to (2.8) into the equations (2.1) and (2.2) leads to

$$\begin{aligned} \nabla \times E &= -\frac{\partial B}{\partial t} = -\frac{\partial(\tilde{B}e^{i\omega t})}{\partial t} = -i\omega\tilde{B}e^{i\omega t} = -i\omega B \\ &= -i\omega\mu H, \end{aligned} \tag{2.9}$$

$$\begin{aligned} \nabla \times H &= J + \frac{\partial D}{\partial t} = J + \frac{\partial(\varepsilon E)}{\partial t} = J + \frac{\varepsilon\partial(\tilde{E}e^{i\omega t})}{\partial t} \\ &= J + i\omega\varepsilon E = J_o + J_s + i\omega\varepsilon E \\ &= (\sigma + i\omega\varepsilon)E + J_s. \end{aligned} \tag{2.10}$$

In EIT, the quasi-static conditions are usually assumed for the simplification of equations (Vauhkonen 1997). That is, $i\omega\mu H$ and $i\omega\varepsilon E$ in the above equations (2.9) and (2.10) can be omitted at the given frequency ω in EIT, and time derivative term in equation (2.3) is set to be zero. On the other hand, the current source J_s is zero inside the object. Therefore, the equation (2.3) and (2.10) can be simplified as

$$E = -\nabla u, \tag{2.11}$$

$$\nabla \times H = \sigma E + J_s. \tag{2.12}$$

Applying the divergence on the above equation (2.12), we get

$$\nabla \cdot (\nabla \times H) = \nabla \cdot J = \nabla \cdot (\sigma E + J_s) = 0. \tag{2.13}$$

Here, the current source J_s is zero inside the object. Substituting the equation (2.11) into the equation (2.13), we get

$$\nabla \cdot (\sigma \nabla u) = \nabla \cdot (\frac{1}{\rho} \nabla u) = 0, \tag{2.14}$$

where $\rho \equiv \sigma^{-1}$ is resistivity. The equation (2.14) is known as the governing equation for EIT. The governing equation is corresponding to the interior of the object.

2.1.2 Boundary conditions

On the boundary of the object $\partial\Omega$, the current source J_s is not zero in EIT. Therefore, the equation (2.13) on the boundary is as follows

$$\nabla \cdot \sigma E = -\nabla \cdot J_s. \tag{2.15}$$

Integrating the equation (2.15) over the volume v,

$$\int_v \nabla \cdot \sigma E dv = -\int_v \nabla \cdot J_s dv. \tag{2.16}$$

Using the divergence theorem, we get

$$\int_S \sigma E \cdot \mathbf{n} dS = -\int_S J_s \cdot \mathbf{n} dS, \tag{2.17}$$

where S is the surface of v, and $\mathbf{n}$ is the unit normal vector. Since $J_s = 0$ inside the object and $E = 0$ outside the object, the equation (2.17) gets the form

$$-\sigma E \cdot \mathbf{n}\big|_{inside} = -J_s \cdot \mathbf{n}\big|_{outside}. \tag{2.18}$$

Using the equation (2.11) in the equation (2.18), the Neumann-type boundary condition is obtained as

$$\sigma \frac{\partial u}{\partial \mathbf{n}} = -J_s \cdot \mathbf{n} \equiv j_n, \tag{2.19}$$

where j_n is the negative normal component of the injected current density J_s.

In EIT, the electrode models are used to represent the boundary conditions for injected currents and measured boundary voltages. There are several electrode

models such as gap model, shunt model, and complete electrode model (Cheng 1989, Somersalo *et al*. 1992, Vauhkonen 1997). The complete electrode model (CEM) is usually used in EIT because it is more realistic and accurate model.

The CEM consists of the following boundary conditions

$$u + z_l \sigma \frac{\partial u}{\partial \mathbf{n}} = U_l, \quad (x, y) \in e_l, \quad l = 1, 2, \cdots, L \tag{2.20}$$

$$\int_{e_l} \sigma \frac{\partial u}{\partial \mathbf{n}} dS = I_l, \quad (x, y) \in e_l, \quad l = 1, 2, \cdots, L \tag{2.21}$$

$$\sigma \frac{\partial u}{\partial \mathbf{n}} = 0, \quad (x, y) \in \partial\Omega \setminus \bigcup_{l=1}^{L} e_l \tag{2.22}$$

where L is the number of electrodes, z_l is the contact impedance between the l th electrode and the surface of an object, U_l is the measured voltage on the l th electrode, and I_l is the injected current into the l th electrode. As represented in the equation (2.20), CEM considers the shunting effect of the electrodes, i.e., the potential on the electrode is constant, as well as the contact impedance between the electrode and the medium. The injected current I_l is known rather than the current density j_n under the electrodes, therefore, the boundary condition (2.19) is rewritten as the equation (2.21). Furthermore, the current density $j_n = 0$ on the gaps between electrodes, so the relation is given in the equation (2.22).

In addition to the electrode model, the following Kirchhoff's laws on the measured voltages and injected currents are needed to guarantee the existence and uniqueness of the solution (Somersalo *et al*. 1992).

$$\sum_{l=1}^{L} I_l = 0 \quad \text{and} \quad \sum_{l=1}^{L} U_l = 0. \tag{2.23}$$

2.1.3 Finite element formulation

The FEM is a numerical method for solving partial differential equations with complicated geometries and non-trivial boundary conditions (Brenner and Scott 1994). The FEM formulation changes a continuous form of the forward problem into

a discrete form. In this thesis, two-dimentsional FEM for CEM is used to solve the forward problem.

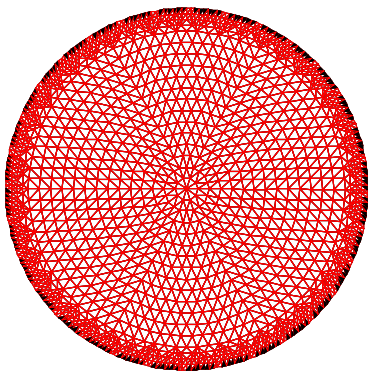

Figure 2.2. Typical FEM mesh structure

In FEM, the object Ω is discretized into small elements as shown in figure 2.2. The vertices of the triangle elements are called the nodes. The black elements are corresponding to the electrodes attached on the circumference of object.

If N_n is the number of nodes of the FEM mesh, the electric potentials u within the object are approximated as u^h, and it is represented as

$$u \equiv u(x,y) \approx u^h(x,y) = \sum_{i=1}^{N_n} \alpha_i \phi_i(x,y), \tag{2.24}$$

and the voltages U on the electrodes are approximated as

$$U \approx U^h = \sum_{j=1}^{L-1} \beta_j \mathbf{m}_j, \tag{2.25}$$

where ϕ_i is the two-dimensional first-order basis function, α_i and β_j are the coefficients to be determined, and $\mathbf{m}_1 = [1,-1,0,\cdots,0]^{\mathrm{T}}$, $\mathbf{m}_2 = [1,0,-1,0,\cdots,0]^{\mathrm{T}} \in \mathbb{R}^{L\times 1}$, etc. This choice for $\mathbf{m}_j$ ensures that the Kirchhoff's voltage law in the equation (2.23) is fulfilled.

Representing the equation (2.25) in a matrix form, the voltages U^h on the electrodes can be expressed as

$$U^h = \begin{bmatrix} U_1^h \\ U_2^h \\ \vdots \\ U_L^h \end{bmatrix} = \mathbf{M}\boldsymbol{\beta} = \begin{bmatrix} 1 & 1 & \cdots & 1 \\ -1 & 0 & \cdots & 0 \\ 0 & -1 & \cdots & 0 \\ \vdots & \vdots & \ddots & \vdots \\ 0 & 0 & \cdots & -1 \end{bmatrix} \begin{bmatrix} \beta_1 \\ \beta_2 \\ \beta_3 \\ \vdots \\ \beta_{L-1} \end{bmatrix} = \begin{bmatrix} \beta_1 + \beta_1 + \cdots + \beta_{L-1} \\ -\beta_1 \\ -\beta_2 \\ \vdots \\ -\beta_{L-1} \end{bmatrix}, \quad (2.26)$$

where $\mathbf{M} = [\mathbf{m}_1 \quad \mathbf{m}_2 \quad \cdots \quad \mathbf{m}_{L-1}]$ and $\boldsymbol{\beta} = [\beta_1 \quad \beta_2 \quad \cdots \quad \beta_{L-1}]^T$.

Let w and W_l be arbitrary weighting functions for the basis function ϕ_i and $\mathbf{M}(l, j) = (\mathbf{m}_j)_l$. Multiplying the governing equation (2.14) by w and integrating it over Ω,

$$\int_\Omega w\nabla \cdot \left(\rho^{-1}\nabla u\right) d\Omega = 0. \quad (2.27)$$

The gradient product rule of terms in equation (2.27) is written as

$$\nabla \cdot \left(w\rho^{-1}\nabla u\right) = \rho^{-1}\nabla w \cdot \nabla u + w\nabla \cdot (\rho^{-1}\nabla u). \quad (2.28)$$

Using the equation (2.28) in the equation (2.27), we have

$$\int_\Omega w\nabla \cdot \left(\rho^{-1}\nabla u\right) d\Omega = \int_\Omega \nabla \cdot \left(w\rho^{-1}\nabla u\right) d\Omega - \int_\Omega \rho^{-1}\nabla w \cdot \nabla u \; d\Omega = 0. \quad (2.29)$$

Therefore,

$$\int_\Omega \rho^{-1}\nabla w \cdot \nabla u \; d\Omega = \int_\Omega \nabla \cdot \left(w\rho^{-1}\nabla u\right) d\Omega. \quad (2.30)$$

Using the divergence theorem,

$$\int_\Omega \rho^{-1}\nabla w \cdot \nabla u \; d\Omega = \int_\Omega \nabla \cdot \left(w\rho^{-1}\nabla u\right) d\Omega = \int_{\partial\Omega} w\rho^{-1} \frac{\partial u}{\partial \mathbf{n}} dS. \quad (2.31)$$

Adding and subtracting $\sum_{l=1}^{L} \int_{e_l} W_l \rho^{-1} \frac{\partial u}{\partial \mathbf{n}} dS$ in the above equation, the equation (2.31) can be written as

$$\int_\Omega \rho^{-1}\nabla w\cdot\nabla u\ d\Omega=\sum_{l=1}^{L}\int_{e_l}(w-W_l)\rho^{-1}\frac{\partial u}{\partial \mathbf{n}}dS+\sum_{l=1}^{L}\int_{e_l}W_l\rho^{-1}\frac{\partial u}{\partial \mathbf{n}}dS. \tag{2.32}$$

Invoking the equation (2.20),

$$\rho^{-1}\frac{\partial u}{\partial \mathbf{n}}=-\frac{u\ -U_l}{z_l}, \tag{2.33}$$

and using equations (2.33) and (2.21), the equation (2.32) can be written as

$$\int_\Omega \rho^{-1}\nabla w\cdot\nabla u\ d\Omega=-\sum_{l=1}^{L}\frac{1}{z_l}\int_{e_l}(u\ -U_l)(w-W_l)dS+\sum_{l=1}^{L}I_lW_l. \tag{2.34}$$

Therefore, we can obtain the weak form of the complete electrode model as follows

$$\int_\Omega \rho^{-1}\nabla u\ \cdot\nabla w d\Omega+\sum_{l=1}^{L}\frac{1}{z_l}\int_{e_l}(u\ -U_l)(w-W_l)dS=\sum_{l=1}^{L}I_lW_l. \tag{2.35}$$

Substituting the equation (2.24) and $U_l^h=\sum_{q=1}^{L-1}\beta_q\mathbf{M}(l,q)$ into u and U_l, respectively, and inserting the FEM basis functions ϕ_i and $\mathbf{M}(l,j)$ to the weak form (2.35), the weak form becomes

$$\begin{aligned}&\sum_{k=1}^{N_n}\left[\int_\Omega \rho^{-1}\nabla\phi_i\cdot\nabla\phi_k d\Omega\right]\alpha_k+\sum_{k=1}^{N_n}\left[\sum_{l=1}^{L}\frac{1}{z_l}\int_{e_l}\phi_i\phi_k dS\right]\alpha_k-\sum_{l=1}^{L}\frac{1}{z_l}\int_{e_l}\phi_iU_l^h dS\\&-\sum_{k=1}^{N_n}\left[\sum_{l=1}^{L}\frac{1}{z_l}\int_{e_l}\mathbf{M}(l,j)\phi_k dS\right]\alpha_k+\sum_{l=1}^{L}\frac{1}{z_l}\int_{e_l}\mathbf{M}(l,j)U_l^h dS=\sum_{l=1}^{L}I_l\mathbf{M}(l,j),\end{aligned} \tag{2.36}$$

$$\begin{aligned}&\sum_{k=1}^{N_n}\left[\int_\Omega \rho^{-1}\nabla\phi_i\cdot\nabla\phi_k d\Omega\right]\alpha_k+\sum_{k=1}^{N_n}\left[\sum_{l=1}^{L}\frac{1}{z_l}\int_{e_l}\phi_i\phi_k dS\right]\alpha_k-\sum_{q=1}^{L-1}\left[\sum_{l=1}^{L}\frac{1}{z_l}\int_{e_l}\phi_i\mathbf{M}(l,q)dS\right]\beta_q\\&-\sum_{k=1}^{N_n}\left[\sum_{l=1}^{L}\frac{1}{z_l}\int_{e_l}\mathbf{M}(l,j)\phi_k dS\right]\alpha_k+\sum_{q=1}^{L-1}\left[\sum_{l=1}^{L}\frac{1}{z_l}\int_{e_l}\mathbf{M}(l,j)\mathbf{M}(l,q)dS\right]\beta_q=\sum_{l=1}^{L}I_l\mathbf{M}(l,j).\end{aligned} \tag{2.37}$$

That is, for any i and q,

$$\sum_{k=1}^{N_n}\left[\int_\Omega \rho^{-1}\nabla\phi_i\cdot\nabla\phi_k d\Omega+\sum_{l=1}^{L}\frac{1}{z_l}\int_{e_l}\phi_i\phi_k dS\right]\alpha_k-\sum_{q=1}^{L-1}\left[\sum_{l=1}^{L}\frac{1}{z_l}\int_{e_l}\phi_i\mathbf{M}(l,q)dS\right]\beta_q=0$$

and (2.38)

$$-\sum_{k=1}^{N_n}\left[\sum_{l=1}^{L}\frac{1}{z_l}\int_{e_l}\mathbf{M}(l,j)\phi_k dS\right]\alpha_k+\sum_{q=1}^{L-1}\left[\sum_{l=1}^{L}\frac{1}{z_l}\int_{e_l}\mathbf{M}(l,j)\mathbf{M}(l,q)dS\right]\beta_q=\sum_{l=1}^{L}I_l\mathbf{M}(l,j).$$

Using the finite element formulation $\mathbf{Ab}=\mathbf{f}$, the above equation can be expressed in a matrix form where each components are defined as below

$$\mathbf{A}=\begin{pmatrix}\mathbf{B} & \mathbf{C}\\ \mathbf{C}^T & \mathbf{D}\end{pmatrix}\in\mathbb{R}^{(N_n+L-1)\times(N_n+L-1)}, \tag{2.39}$$

$$\mathbf{b}=\begin{pmatrix}\boldsymbol{\alpha}\\ \boldsymbol{\beta}\end{pmatrix}\in\mathbb{R}^{N_n+L-1}, \tag{2.40}$$

$$\mathbf{f}=\begin{pmatrix}\mathbf{0}\\ \sum_{l=1}^{L}I_l\mathbf{M}(l,j)\end{pmatrix}=\begin{pmatrix}\mathbf{0}\\ \mathbf{M}^T I\end{pmatrix}=\begin{pmatrix}\mathbf{0}\\ \breve{\mathbf{I}}\end{pmatrix}\in\mathbb{R}^{N_n+L-1}, \tag{2.41}$$

where

$$\mathbf{B}(i,j)=\int_\Omega\rho^{-1}\nabla\phi_i\cdot\nabla\phi_j d\Omega+\sum_{l=1}^{L}\frac{1}{z_l}\int_{e_l}\phi_i\phi_j dS, \tag{2.42}$$

$$i,j=1,2,\cdots,N_n$$

$$\mathbf{C}(i,j)=-\left(\frac{1}{z_1}\int_{e_1}\phi_i dS-\frac{1}{z_{j+1}}\int_{e_{j+1}}\phi_i dS\right), \tag{2.43}$$

$$i=1,2,\cdots,N_n \text{ and } j=1,2,\cdots,L-1$$

$$\mathbf{D}(i,j)=\sum_{l=1}^{L}\frac{1}{z_l}\int_{e_l}\mathbf{m}_i\mathbf{m}_j dS$$

$$=\begin{cases}\dfrac{|e_1|}{z_1}, & i\neq j,\quad i,j=1,2,\cdots,L-1\\ \dfrac{|e_1|}{z_1}+\dfrac{|e_{j+1}|}{z_{j+1}}, & i=j\end{cases} \tag{2.44}$$

where $|e_j|$ is the area of the j th electrode. Also, in the equation (2.41), $\mathbf{0} \in \mathbb{R}^{N_n}$, $I = [I_1, I_2, \cdots, I_L]^{\mathrm{T}} \in \mathbb{R}^L$ and $\breve{\mathbf{I}} = [I_1 - I_2, I_1 - I_3, \cdots, I_1 - I_L]^{\mathrm{T}} \in \mathbb{R}^{L-1}$, and the vector I is called current pattern. Therefore, the approximate solutions u^h and U^h for the forward problem are obtained by solving $\mathbf{b} = \mathbf{A}^{-1}\mathbf{f}$. That is, the last $L-1$ coefficients in $\mathbf{b}$ give the referenced voltages on the electrodes.

2.1.4 Current injection methods for the data collection

In this thesis, we focus on static cases where the internal resistivity distribution of the object is not changed within the time taken to acquire a single frame of measurement data induced from all the independent current patterns. The current is injected between two of the electrodes or to all electrodes, and then the voltages are measured between two of the electrodes or from all the electrodes with respect to one reference.

Current injection method can affect the reconstruction performance depending on each internal situation termed as sensitivity. Various methods have been studied for the current injection (Isaacson 1986, Cheng *et al*. 1988, Webster *et al*. 1990, Cheney and Isaacson 1992). In EIT, the most common current injection methods are the adjacent method, the opposite method, and the trigonometric method. The number of independent current patterns is decided by the number of electrodes and the current patterns.

In the adjacent method, currents are injected through two adjacent electrodes, e.g. $I_1 = I_0$, $I_2 = -I_0$, and the voltages are measured from all the pairs of electrodes. This is repeated for all the current patterns. For example, with 16 electrodes the number of voltage measurement data is $16 \times 16 = 256$. This method produces non-uniform current density because the injected currents are spread near the boundary. That is, this will diminish the sensitivity of the voltage measurements with respect to the resistivity changes at the center of the object.

In the opposite method, a pair of diametrically opposed electrodes is selected to inject current, e.g. the current pattern for the electrode pair (e_1, e_9) with 16 electrodes will be ($I_1 = I_0$, $I_9 = -I_0$). The voltages are measured using one reference electrode. The number of voltage measurement data is $16 \times 8 = 128$ since the number of

independent current patterns is 8. This method has more uniform density compared to the adjacent method.

As for the trigonometric method, the currents with appropriate magnitude flow through all the electrodes simultaneously. The voltages are obtained with respect to a single grounded electrode. The injected trigonometric current is defined on the l th electrode at k th pattern as

$$I_l^k = \begin{cases} I_0 \cos(k\theta_l), & l = 1,2,\cdots,L,\ k = 1,2,\cdots,\dfrac{L}{2} \\ I_0 \sin(k\theta_l - \dfrac{L}{2}\theta_l), & l = 1,2,\cdots,L,\ k = \dfrac{L}{2}+1,\cdots,L-1 \end{cases} \tag{2.45}$$

where $\theta_l = 2\pi l / L$. This method is known as the best current injection method to distinguish a target placed at the center of the domain.

2.2 Inverse problem

2.2.1 Gauss-Newton algorithm

The relation for the voltages on boundary electrodes U and internal resistivity distribution ρ is a nonlinear function, so the measured voltages $\tilde{U}$ can be written using the measurement errors ξ_m as

$$\tilde{U} = U(\rho) + \xi_m, \tag{2.46}$$

where $\tilde{U}$, $U(\rho)$ and $\xi_m \in \mathbb{R}^{N_m}$ and $\rho \in \mathbb{R}^{N_e}$. N_m is the number of independent voltage data, and N_e is the number of FEM elements. For the estimated resistivity distribution $\hat{\rho}$, the measured voltages using the residual errors $\xi_r \in \mathbb{R}^{N_m}$ also can be written as

$$\tilde{U} = U(\hat{\rho}) + \xi_r. \tag{2.47}$$

The general inverse problem approach for estimating the internal resistivity distribution is represented as a least squares problem. In the least squares problem,

the estimated resistivity distribution $\hat{\rho}$ that minimizes the $l2$-norm of the residual errors is selected as an optimal choice for the internal resistivity distribution ρ. The objective function to find the optimal estimates $\hat{\rho}$ is given by

$$\begin{aligned}\Phi = \Phi(\hat{\rho}) &= \frac{1}{2}\left\|\xi_r\right\|^2 = \frac{1}{2}\xi_r{}^T\xi_r \\ &= \frac{1}{2}\left[\tilde{U} - U(\hat{\rho})\right]^T\left[\tilde{U} - U(\hat{\rho})\right].\end{aligned} \tag{2.48}$$

Let $\hat{\rho} = \rho_c + \Delta\rho$, where ρ_c is the estimated current resistivity distribution which can converge to least squares estimates and $\Delta\rho$ is sufficiently small value. Linearizing $U(\hat{\rho})$ at ρ_c using a first-order Taylor series expansion,

$$U(\hat{\rho}) \approx U(\rho_c) + H\Delta\rho, \tag{2.49}$$

where $H \equiv H(\rho_c) \equiv \dfrac{\partial U(\rho_c)}{\partial \rho_c} \in \mathbb{R}^{N_m \times N_e}$ is the Jacobian matrix. The measurement residual error can be linearly approximated as

$$\begin{aligned}\xi_r \equiv \Delta U \equiv \tilde{U} - U(\hat{\rho}) &\approx \tilde{U} - U(\rho_c) - H\Delta\hat{\rho} \\ &= \Delta U_c - H\Delta\rho,\end{aligned} \tag{2.50}$$

where $\Delta U_c \equiv \tilde{U} - U(\rho_c)$. The above objective function can be written as

$$\Phi(\hat{\rho}) \approx \Phi(\Delta\rho) = \frac{1}{2}\left[\Delta U_c - H\Delta\rho\right]^T\left[\Delta U_c - H\Delta\rho\right]. \tag{2.51}$$

To find the global minimum of the quadratic function of equation (2.51), the differentiation of the equation (2.51) is set to zero as

$$\nabla_{\Delta\rho}\Phi \equiv \Phi'(\Delta\rho) = H^T H\Delta\rho - H^T\Delta U_c = 0. \tag{2.52}$$

From the above equation, we have the following equation

$$H^T H\Delta\rho = H^T\Delta U_c. \tag{2.53}$$

If the $H^T H$ called Hessian matrix is positive definite, then $H^T H$ can be inverted to obtain the solution for the optimal estimate as

$$\Delta\rho = (H^T H)^{-1} H^T \Delta U_c. \tag{2.54}$$

Using $\hat{\rho} = \rho_c + \Delta\rho$ and $\Delta U_c \equiv \tilde{U} - U(\rho_c)$, Gauss-Newton algorithm can be obtained as

$$\hat{\rho} = \rho_c + (H^T H)^{-1} H^T (\tilde{U} - U(\rho_c)). \tag{2.55}$$

Also, using iterative index i, the above equation can be rewritten as

$$\hat{\rho}_{i+1} = \hat{\rho}_i + (H_i^T H_i)^{-1} H_i^T (\tilde{U} - U(\hat{\rho}_i)). \tag{2.56}$$

The Hessian matrix ($H_i^T H_i$) in the equation (2.56) is highly ill-posed. So, in order to give the stability of inverse solution and the meaningful solution, the regularization method as a penalty or *prior* information has to be used in the equation (2.56). As for the regularization methods in EIT, it will be reviewed and described in chapter 3.

2.2.2 Computation of Jacobian

Forward solution and Jacobian have to be calculated iteratively in the Gauss-Newton algorithm given in the equation (2.56). Jacobian means the rate of change of voltages with respect to the internal resistivity distribution, and the Jacobian matrix is defined as

$$H = \begin{bmatrix} \frac{\partial U^{(1)}}{\partial \rho_1} & \cdots & \frac{\partial U^{(1)}}{\partial \rho_{N_e}} \\ \vdots & \ddots & \vdots \\ \frac{\partial U^{(K)}}{\partial \rho_1} & \cdots & \frac{\partial U^{(K)}}{\partial \rho_{N_e}} \end{bmatrix}, \tag{2.57}$$

where $U^{(k)} \in \mathbb{R}^L$ is induced by k th current pattern.

The Jacobian matrix can be computed by the standard method (Yorkey and Webster 1987, Vauhkonen 1997). From the formulation of FEM $\mathbf{Ab} = \mathbf{f}$, the n th column of the Jacobian matrix H can be obtained from

$$\frac{\partial \mathbf{b}}{\partial \rho_n} = \frac{\partial \mathbf{A}^{-1}\mathbf{f}}{\partial \rho_n} = -\mathbf{A}^{-1}\frac{\partial \mathbf{A}}{\partial \rho_n}\mathbf{A}^{-1}\mathbf{f} = -\mathbf{A}^{-1}\frac{\partial \mathbf{A}}{\partial \rho_n}\mathbf{b}. \tag{2.58}$$

The derivative $\frac{\partial \mathbf{A}}{\partial \rho_n}$ is related to only the matrix $\mathbf{B}$ in $\mathbf{A}$. So, the derivative $\frac{\partial \mathbf{A}}{\partial \rho_n}$ can be obtained as

$$\frac{\partial \mathbf{A}(m,i)}{\partial \rho_n} = -\frac{1}{\rho_n^2}\int_{\Delta_n} \nabla \varphi_m \cdot \nabla \varphi_i dxdy, \tag{2.59}$$

where Δ_n denotes the element with which the derivative is calculated.

The equation (2.58) forms the derivatives of all the voltages with respect to ρ_n. So, the part of voltages on the electrodes has to be extracted. Consider an extracting matrix below

$$\widehat{\mathbf{M}} = [\mathbf{0} \quad \mathbf{M}], \tag{2.60}$$

where $\mathbf{0} \in \mathbb{R}^{L \times N_n}$, $\mathbf{M} \in \mathbb{R}^{L \times (L-1)}$. As for k th current pattern, using equations (2.60) and (2.40), the voltages $U^{(k)} = \mathbf{M\beta}$ on the electrodes are expressed as

$$U^{(k)} = \mathbf{M\beta} = \widehat{\mathbf{M}}\mathbf{b}. \tag{2.61}$$

Therefore, the derivatives $\frac{\partial U^{(k)}}{\partial \rho_n}$ can be obtained as

$$\frac{\partial U^{(k)}}{\partial \rho_n} = \frac{\partial (\widehat{\mathbf{M}}\mathbf{b})}{\partial \rho_n} = \widehat{\mathbf{M}}\frac{\partial \mathbf{b}}{\partial \rho_n} = -\widehat{\mathbf{M}}\mathbf{A}^{-1}\frac{\partial \mathbf{A}}{\partial \rho_n}\mathbf{b}. \tag{2.62}$$

3. Regularization Methods in EIT

EIT inverse problem is a discrete ill-posed problem due to its nonlinear behaviour of measured voltage and inner resistivity distribution. In the discrete ill-posed problem, the regularization has to be used to stabilize the problem and provide the meaningful solution.

In this chapter, the requirement of the regularization and three regularization methods widely used in EIT are introduced. In section 3.1, the need of the regularization in discrete ill-posed problem is introduced. Three regularization methods such as the $l1$-norm, $l2$-norm and total variation (TV) are reviewed in section 3.2. Also, the numerical simulations for comparison of three regularization methods are presented in section 3.3.

3.1 Why the regularization is necessary in discrete ill-posed problem?

Consider the following discrete linear model

$$Y^{exact} = FX^{exact}, \tag{3.1}$$

where $X^{exact} \in \mathbb{R}^n$, $Y^{exact} \in \mathbb{R}^m$, and $F \in \mathbb{R}^{m \times n}$ with $m \geq n$. The measurement data Y includes noise e and the naive solution X^{naive} can be solved by the least squares problem represented as $\min_X \|Y - FX\|^2$. And the solution is given by

$$X^{naive} = (F^T F)^{-1} F^T Y. \tag{3.2}$$

As one method for finding inversion matrix, the singular value decomposition (SVD) can be used. Using SVD, the matrix F is decomposed of the form

$$F = \mathbf{U}\Sigma\mathbf{V}^T = \sum_{i=1}^{n} \mathbf{u}_i \lambda_i \mathbf{v}_i^T, \tag{3.3}$$

where $\mathbf{U} = [\mathbf{u}_1, \cdots, \mathbf{u}_n] \in \mathbb{R}^{m \times n}$ and $\mathbf{V} = [\mathbf{v}_1, \cdots, \mathbf{v}_n] \in \mathbb{R}^{n \times n}$ are matrices with orthonormal columns $\mathbf{u}_i \in \mathbb{R}^m$ and $\mathbf{v}_i \in \mathbb{R}^n$, respectively, and $\Sigma = diag[\lambda_1, \cdots, \lambda_n]$ has non-negative diagonal elements in decreasing order, that is, $\lambda_1 \geq \cdots \geq \lambda_n \geq 0$.

Using the equation (3.3) with $\mathbf{U}^T\mathbf{U} = \mathbf{V}^T\mathbf{V} = \mathbf{I} \in \mathbb{R}^{n \times n}$, the naive solution X^{naive} in the equation (3.2) can be rewritten by

$$X^{naive} = \sum_{i=1}^{n} \frac{\mathbf{u}_i^T Y}{\lambda_i} \mathbf{v}_i = \sum_{i=1}^{n} \frac{\mathbf{u}_i^T (Y^{exact} + e)}{\lambda_i} \mathbf{v}_i. \tag{3.4}$$

The naive solution in the equation (3.4) is dominated by the smallest singular value λ_n. If the singular values of F are close to zero and the condition number, i.e., the ratio between the largest and the smallest nonzero singular values, is large, then F is rank-deficiency and ill-conditioned. This inverse problem is called discrete ill-posed problem (Hansen 1994, Fuhry and Reichel 2012). In the discrete ill-posed problem, the naive solution is potentially very sensitive to error e and tends to have many sign changes and appear randomly. Even if there is no error in the measurement data Y, the discrete ill-posed problem has numerically unstable naive solution. That is, the naive solution is far from the exact solution as shown in figure 3.1 and then it can be useless.

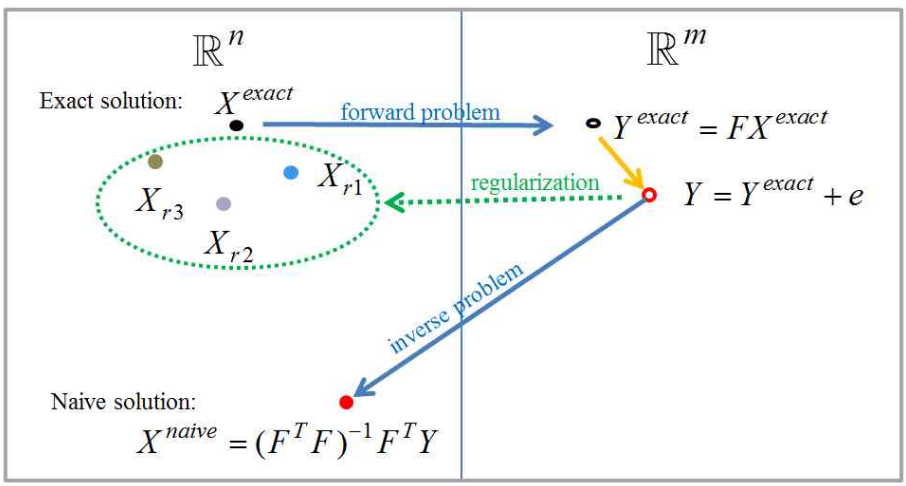

Figure 3.1. The requirement of regularization in the discrete ill-posed problem

In the discrete ill-posed problem, specific techniques called the regularization method to find a stable solution have to be used as an additional term in the least

squares problem. The regularization method can be formulated based on the *prior* information. That is, the regularization method can replace ill-posed inverse problem by a nearby well-posed problem, and it gives efficient and numerically stable methods that lead to a useful solution. Hence, the regularized solution (X_r) provides a good approximation to the exact solution as shown in figure 3.1.

3.2 Three regularization methods in EIT

Recall equations (2.48) and (2.56). The objective function to estimate internal resistivity distribution in EIT is rewritten as

$$\Phi = \frac{1}{2}\left\|\tilde{U} - U(\hat{\rho})\right\|^2, \tag{3.5}$$

and the iterative naive solution is given by

$$\hat{\rho}_{i+1} = \hat{\rho}_i + (H_i^T H_i)^{-1} H_i^T (\tilde{U} - U(\hat{\rho}_i)). \tag{3.6}$$

The Jacobian matrix $H \in \mathbb{R}^{N_m \times N_e}$ is rank-deficient and ill-conditioned, that is, the Hessian Matrix ($H^T H$) is highly ill-posed. The main reason of ill-posed nature in EIT is resulted from the fact that the number of unknown resistivity elements is generally much larger than the number of independent measured voltage data as well as by the fact that the relation between voltages and resistivity distribution is non-linear (Dai 2008). Hence, the naive solution in the equation (3.6) is unstable and it has large changes caused by small changes in the measurement data. In order to mitigate the ill-posed problem, the equation (3.6) should be regularized by adding an additional term in the equation (3.5). The regularized objective function can be written as

$$\Phi = \frac{1}{2}\left\|\tilde{U} - U(\hat{\rho})\right\|^2 + R(\hat{\rho} - \rho_*), \tag{3.7}$$

where $R(\hat{\rho} - \rho_*)$ is a regularizing penalty function and ρ_* is a *priori* estimate of ρ .

The reconstruction solution has different performance depending on the type of the regularization method used in the equation (3.7), i.e., the regularization method plays

an important role in the spatial resolution. A brief description of the typical three regularization methods used in EIT is described and compared in the following subsection.

3.2.1 The *l*2-norm regularization method

In the equation (3.7), the regularizing penalty function is commonly used as

$$R(\hat{\rho}-\rho_*)=\frac{1}{2}\gamma\left\|\hat{\rho}-\rho_*\right\|^2_{\Gamma^T\Gamma}, \tag{3.8}$$

where $\|\cdot\|^2$ denotes the *l*2-norm, Γ is a regularization matrix or a regularization operator, γ is a regularization parameter.

The objective function with the *l*2-norm regularization method can be written as

$$\Phi_{l2}(\hat{\rho})=\frac{1}{2}\left\|\tilde{U}-U(\hat{\rho})\right\|^2+\frac{1}{2}\gamma\left\|\hat{\rho}-\rho_*\right\|^2_{\Gamma^T\Gamma}. \tag{3.9}$$

The regularized solution minimizing the equation (3.9) can be derived in a similar fashion as shown in chapter 2. Linearizing the above equation (3.9) has the form

$$\begin{aligned}\Phi_{l2}(\hat{\rho})\approx\Phi_{l2}(\Delta\rho)=&\frac{1}{2}\left[\Delta U_c-H\Delta\rho\right]^T\left[\Delta U_c-H\Delta\rho\right]\\&+\frac{1}{2}\gamma\left[\Delta\rho+\rho_c-\rho_*\right]^T\Gamma^T\Gamma\left[\Delta\rho+\rho_c-\rho_*\right].\end{aligned} \tag{3.10}$$

The differentiation of the equation (3.10) is set to zero as

$$\Phi'_{l2}(\Delta\rho)=H^TH\Delta\rho-H^T\Delta U+\gamma\Gamma^T\Gamma\Delta\rho+\gamma\Gamma^T\Gamma(\rho_c-\rho_*)=0. \tag{3.11}$$

From the above equation,

$$\Delta\rho=(H^TH+\gamma\Gamma^T\Gamma)^{-1}[H^T\Delta U-\gamma\Gamma^T\Gamma(\rho_c-\rho_*)]. \tag{3.12}$$

where $H^TH+\gamma\Gamma^T\Gamma$ is positive definite. Therefore, the regularized solution can be obtained from iterative Gauss-Newton algorithm with the *l*2-norm regularization method,

$$\hat{\rho}_{i+1} = \hat{\rho}_i + (H_i^T H_i + \gamma \Gamma^T \Gamma)^{-1} \{H_i^T [\tilde{U} - U(\hat{\rho}_i)] - \gamma \Gamma^T \Gamma (\hat{\rho}_i - \rho_*)\}. \quad (3.13)$$

In the *l*2-norm regularization method, the *prior* estimate ρ_* is generally set to zero, therefore, the equation (3.13) takes the form

$$\hat{\rho}_{i+1} = \hat{\rho}_i + (H_i^T H_i + \gamma \Gamma^T \Gamma)^{-1} \{H_i^T [\tilde{U} - U(\hat{\rho}_i)] - \gamma \Gamma^T \Gamma \hat{\rho}_i\}. \quad (3.14)$$

The regularization matrix Γ in the equation (3.14) is properly chosen to achieve good reconstruction performance. Commonly, it uses an identity matrix (Yorkey *et al*. 1987) called standard Tikhonov regularization method, a positive diagonal matrix (Cheney *et al*. 1990) called NOSER (Newton's one-step error reconstructor) prior, difference-type regularization matrix (Hua *et al*. 1988) called generalized Tikhonov regularization method ($\Gamma \neq \mathbf{I}$).

The regularization parameter γ controls the amount of regularization. Choosing proper regularization parameter is very important to have a good reconstruction performance. There are several methods for the choice of this regularization parameter. The most common methods are the L–curve method (Hansen 1992, Hanke 1996), the generalized cross validation method (Golub *et al.* 1979), and *ad hoc* method adjusting *a posteriori* by visual examination. The *ad hoc* approach is commonly used in EIT, and the method is adopted in this thesis.

In the standard Tikhonov regularization matrix, since $\Gamma^T \Gamma = \mathbf{I}$, the condition number of $H^T H + \gamma \mathbf{I}$ can be written

$$cond(H^T H + \gamma \mathbf{I}) = \frac{\lambda_1 + \gamma}{\lambda_n + \gamma}, \quad (3.15)$$

where λ_i is ith singular value. If λ_n is very small, the above equation is close to $\lambda_1 / \gamma + 1$. For a large γ even if H does not have full rank, it can be seen that the inversion term in the equation (3.14) is well-posed.

In the NOSER prior, $\Gamma^T \Gamma$ is considered to be diagonal of the Hessian matrix $H^T H$ with respect to the linearization point ρ_h. Where ρ_h is the best homogenous resistivity distribution which minimizes the *l*2-norm between measured and calculated voltages.

In the generalized Tikhonov regularization method, the regularization matrix Γ is related to the FEM discretization of the computation domain. The resistivity distribution is estimated in element basis, so it is parameterized such that

$$\rho(x,y) = \sum_{k=1}^{N_e} \rho_k \chi_k(x,y), \tag{3.16}$$

where $\chi_k(x,y)$ is the characteristic function of the k th FEM element. The gradient of the resistivity of the k th element can be approximated as the differences in the resistivity of k th element and those of neighboring elements. If the FEM mesh has triangular elements, for inner elements except the boundary, each element has three elements with common edge.

Therefore, k th row of difference matrix Γ for the inner elements can be used commonly as (Heikkinen *et al*. 2001, Kim *et al.2*001, Holder 2005, Yang *et al*. 2014)

$$\Gamma_k = [0,\cdots,0,-1,0,\cdots,0,-1,0,\cdots,0,3,0,\cdots,0,-1,0,\cdots,0], \tag{3.17}$$

where 3 is placed in the k th column and -1 s are allocated in the columns corresponding to the adjacent elements of the k th element. The weight 3 is given with the absolute value of the weight -1 's sum. If the element k is on the boundary, the k th element has only two adjacent elements, then the 3 is replaced by 2 in Γ_k. Therefore, Γ_k for k th element on the boundary can be written as

$$\Gamma_k = [0,\cdots,0,-1,0,\cdots,0,-1,0,\cdots,0,2,0,\cdots,0,0,0,\cdots,0]. \tag{3.18}$$

The l2-norm regularization method penalizes sudden variation in the resistivity to stabilize the inverse problem in EIT. This method gives a good convergence of the invese problem since it gives the smoothing effect. However, it prevents sharp transitions on the boundary between target and background (Borsic *et al*. 2007, Dai and Adler 2008). To preserve sharp transitions, the l1-norm and TV regularization methods in following subsection are adapted to EIT reconstruction problem

3.2.2 The *l*1-norm regularization method

The *l*1-norm regularization method as a penalty function uses $\|\cdot\|^1$ instead of $\|\cdot\|^2$, and the objective function with the *l*1-norm regularization method can be written as

$$\Phi_{l1}(\hat{\rho}) = \frac{1}{2}\left\|\tilde{U} - U(\hat{\rho})\right\|^2 + \frac{1}{2}\gamma\left\|(\hat{\rho} - \rho_*)\right\|^1_{\Gamma^T\Gamma}. \tag{3.19}$$

The above equation is linearized and can be reformulated in a quadratic form

$$\begin{aligned}\Phi_{l1}(\hat{\rho}) \approx \Phi_{l1}(\Delta\rho) = &\frac{1}{2}\left[\Delta U_c - H\Delta\rho\right]^T\left[\Delta U_c - H\Delta\rho\right] \\ &+ \frac{1}{2}\gamma\left[D_\rho(\Delta\rho + \rho_c - \rho_*)\right]^T\Gamma^T\Gamma\left[D_\rho(\Delta\rho + \rho_c - \rho_*)\right],\end{aligned} \tag{3.20}$$

where D_ρ is a diagonal matrix in which

$$\left[D_\rho\right]_{j,j} = (\left[\left|\hat{\rho} - \rho_*\right|\right]_j + \delta)^{-\frac{1}{2}}, \tag{3.21}$$

where δ is a small positive value to maintain differentiability when $\hat{\rho} = \rho_*$.

Assume that $\rho_* = \rho_c$, the regularized solution minimizing the above equation (3.20) can be written as

$$\hat{\rho}_{i+1} = \hat{\rho}_i + (H_i{}^T H_i + \gamma D_\rho{}^T\Gamma^T\Gamma D_\rho)^{-1}(H_i{}^T[\tilde{U} - U(\hat{\rho}_i)]). \tag{3.22}$$

3.2.3 Total variation regularization method

In the total variation (TV) regularization method, the constraint that the total variations in resistivity distribution is assumed zero and is added in the original objective function. The objective function with the TV regularization method is given by

$$\Phi_{TV}(\hat{\rho}) = \frac{1}{2}\left\|\tilde{U} - U(\hat{\rho})\right\|^2 + \frac{1}{2}\gamma\mathrm{TV}(\hat{\rho}). \tag{3.23}$$

In EIT using FEM, the total variations of the resistivity distribution can be defined as the sum of the variations of two elements across each edge weighted by its length. The TV regularization can be expressed as

$$\gamma \mathrm{TV}(\hat{\rho}) = \gamma \sum_{k=1}^{N_l} l_k \left| \hat{\rho}(m) - \hat{\rho}(n) \right| = \gamma \sum_{k=1}^{N_l} \left| \mathbf{L}_k \hat{\rho} \right|, \tag{3.24}$$

here N_l is the number of the edge of FEM, and l_k is the length of k th edge, and m and n are indices of the elements having the common edge k. Also the k th row of TV operator $\mathbf{L}$ can be written as

$$\mathbf{L}_k = [0, \cdots, 0, l_k, 0, \cdots, -l_k, 0, \cdots, 0]. \tag{3.25}$$

The equation (3.24) can be expressed in matrix form as

$$\gamma \mathbf{TV}(\hat{\rho}) = \gamma \left\| \mathbf{L}\hat{\rho} \right\|^1. \tag{3.26}$$

Consequently, the TV regularization method becomes one of the $l1$-norm regularization methods. The objective function with the TV regularization method can be written as

$$\Phi_{TV}(\hat{\rho}) = \frac{1}{2} \left\| \tilde{U} - U(\hat{\rho}) \right\|^2 + \frac{1}{2} \gamma \left\| \mathbf{L}\hat{\rho} \right\|^1. \tag{3.27}$$

The regularized solution minimizing equation (3.27) can be expressed as (Borsic *et al*. 2007)

$$\hat{\rho}_{i+1} = \hat{\rho}_i + (H_i{}^T H_i + \gamma \mathbf{L}^T D_{TV}{}^{-1} \mathbf{L})^{-1} (H_i{}^T [\tilde{U} - U(\hat{\rho}_i)] - \gamma \mathbf{L}^T D_{TV}{}^{-1} \mathbf{L}\hat{\rho}_i), \tag{3.28}$$

where D_{TV} is a diagonal matrix in which

$$[D_{TV}]_{k,k} = \left[\sqrt{(\mathbf{L}_k \hat{\rho}_i)^2 + \delta} \right], \tag{3.29}$$

here δ is a small positive value to maintain differentiability when $\hat{\rho}_i(m) = \hat{\rho}_i(n)$.

3.3. Comparison of three regularization methods

Numerical simulations are performed to compare the performance of the above three regularization methods. Two-phase flow imaging is considered using an industrial process pipe that has a radius of 4 cm . This work is reference to the paper by Kang and Kim published in Journal of IKEEE on 2016 (Kang and Kim 2016).

3.3.1 Simulation conditions

To perform numerical simulations, a circular domain that has 32 electrodes with a width of 0.6 cm is used, and the two different meshes are used to avoid the inverse crime as shown figure 3.2. The true voltages are generated using the unstructured mesh with 4472 triangular elements and 2365 nodes (figure 3.2(a)). The calculated voltages and the estimate of the resistivity distribution are obtained using the structured mesh with 3104 elements and 1681 nodes (figure 3.2(b)).

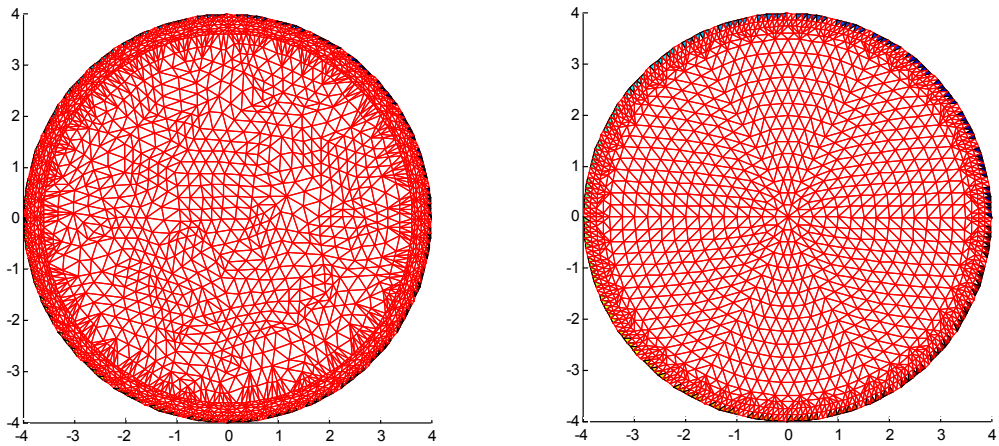

(a) (b)

Figure 3.2. Finite element mesh used for two-phase flow imaging: (a) unstructured mesh and (b) structured mesh

The background is considered to be liquid with a resistivity value of 400 Ωcm and the targets with a radius of 1 cm are considered to be voids with a resistivity value of 800 Ωcm . Two scenarios are considered. One scenario has two targets located near the boundary and the other scenario has two targets located near the center. The cases with and without noise are also examined to compare the reconstruction performance by three regularization methods. With noise case, 1%

relative white Gaussian noise of the generated voltages is added. As a current injection method, trigonometric current patterns are used.

The reconstructed images of numerical simulations are compared using three regularizations such as the $l2$-norm, $l1$-norm, and TV regularization methods described by the equations (3.14), (3.22) and (3.28), respectively. The values of regularization parameter γ for numerical simulations are chosen for each regularization method that gives the best reconstruction performance. The values are shown in table 3.1. Also, the small positive value δ is set to 10^{-6}. The difference matrix using equation (3.17) is used in as $l2$-norm, $l1$-norm regularization methods and TV operator using equation (3.25) is used in the TV regularization method.

Table 3.1. The values of regularization parameter γ for numerical simulations

Noise	Index	$l2$-norm	$l1$-norm	TV
0%	Scenario 1	10^{-4}	10^{-4}	10^{-4}
	Scenario 2	10^{-5}	10^{-3}	10^{-4}
1%	Scenario 1	10^{-2}	10^{-0}	10^{-1}
	Scenario 2	10^{-2}	10^{-0}	10^{-1}

(http://dx.doi.org/10.7471/ikeee.2016.20.3.226)

3.3.2 Performance evaluation index

To compare the estimation performances, the image error (IE) is used as a performance evaluation index (Yang and Peng 2003) and it is defined as follows

$$\mathrm{IE} = \frac{\|\rho - \hat{\rho}\|}{\|\rho\|}. \tag{3.30}$$

It should be noticed that the smaller IE corresponds to better estimation performance.

3.3.3 Numerical results and discussion

Figures 3.3 and 3.4 show the true and reconstructed images for each scenario without noise. The true images are shown in figures 3.3(a) and 3.4(a). The reconstructed images are obtained after 10 iterations using each method, and they are shown in

figures 3.3(b-d) and figures 3.4(b-d). The black circles in figures 3.7 and 3.8 represent the true position of the targets. Figure 3.5 shows the true and estimated resistivity values of each regularization method along the center line in true images. Figure 3.6 shows image errors without noise to evaluate the estimated performance of three regularization methods for each scenario.

Figure 3.7 and figure 3.8 show the true and reconstructed images for each scenario with 1% noise. The true images are shown in figures 3.7(a) and 3.8(a). The reconstructed images are shown in figures 3.7(b-d) and figures 3.8(b-d). The true position of the targets are represented by the black circles in figures 3.7 and 3.8. Figure 3.9 shows the true and estimated resistivity values of each regularization method along the center line in true images. Figure 3.10 shows image errors in the scenarios with 1% noise.

Numerical results show the $l2$-norm regularization has rapid convergence as compared to the other regularization methods. Therefore, it can be said the $l2$-norm regularization method is suitable for one-step algorithms. In without noise case, TV regularization method has the better reconstruction performance with sharp transition in resistivity distribution between target and background as well as preserves discrete change in the resistivity distribution. From the reconstructed results in the presence of noise, for targets close to each other, the $l1$-norm regularization method is found to have better reconstruction performance. For scenario 1 with targets located close to the boundary, TV has better reconstruction performance and the $l1$-norm and $l2$-norm regularization methods are found to have similar reconstruction performance.

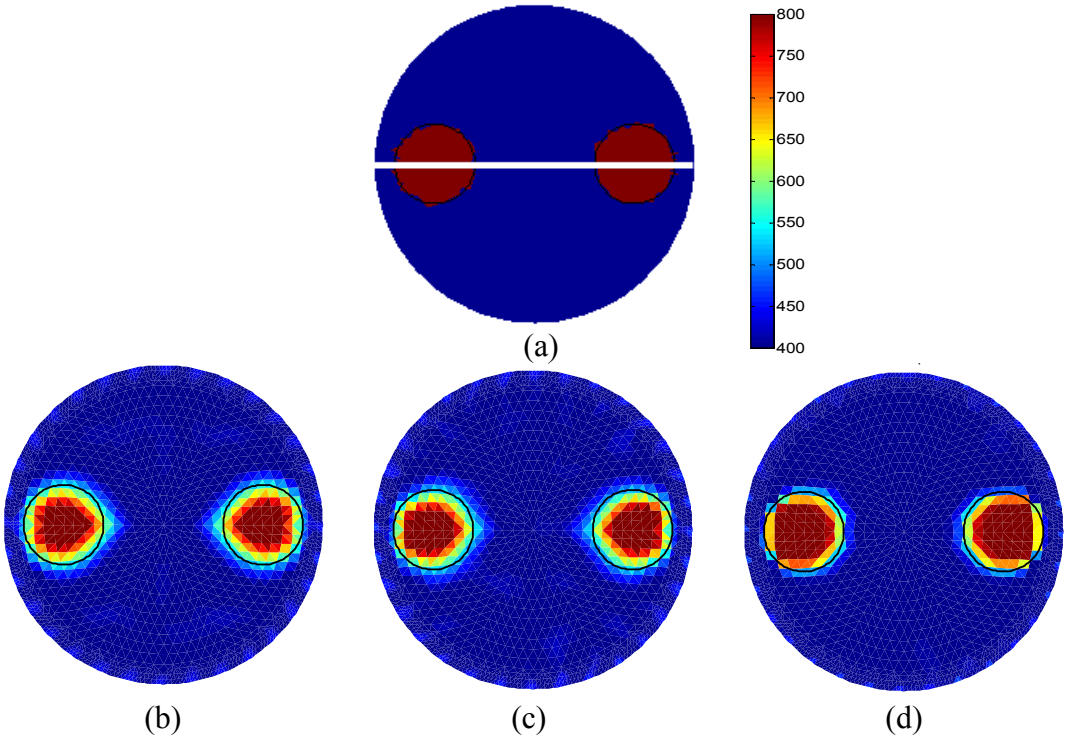

(a) (b) (c) (d)

Figure 3.3. Images for scenario 1 without noise: (a) true image, (b) ~ (d) the reconstructed images by the *l*2-norm, *l*1-norm, and TV regularization methods, respectively.
(http://dx.doi.org/10.7471/ikeee.2016.20.3.226)

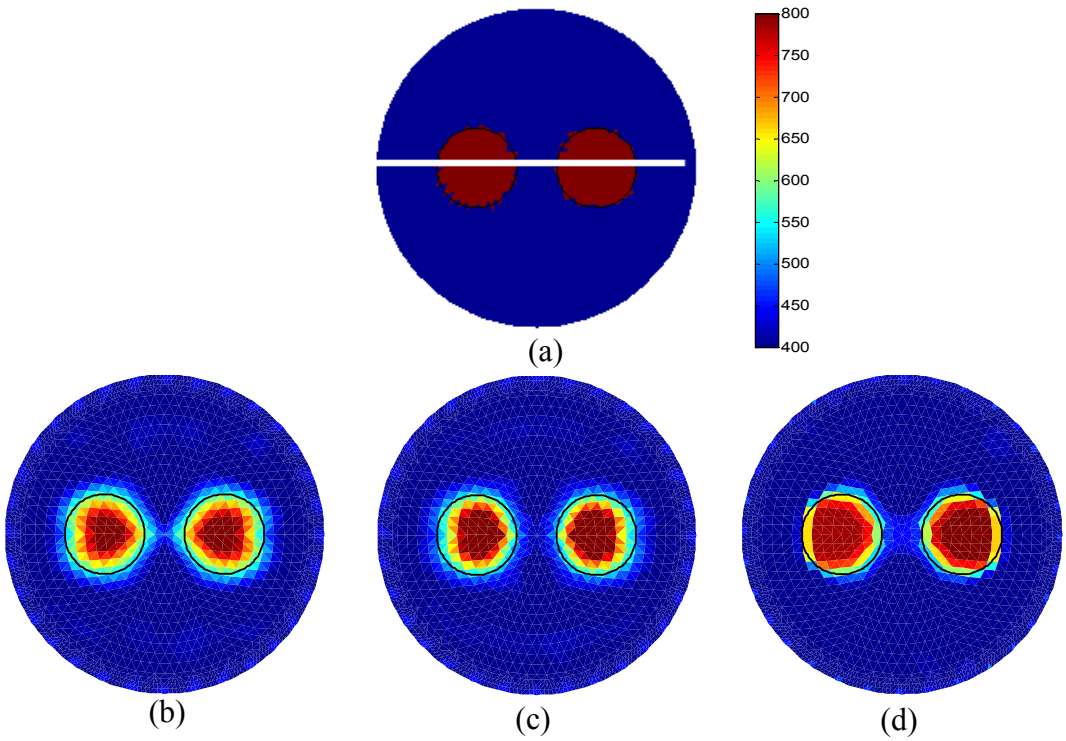

(a) (b) (c) (d)

Figure 3.4. Images for scenario 2 without noise: (a) true image, (b) ~ (d) the reconstructed images by the *l*2-norm, *l*1-norm, and TV regularization methods, respectively.
(http://dx.doi.org/10.7471/ikeee.2016.20.3.226)

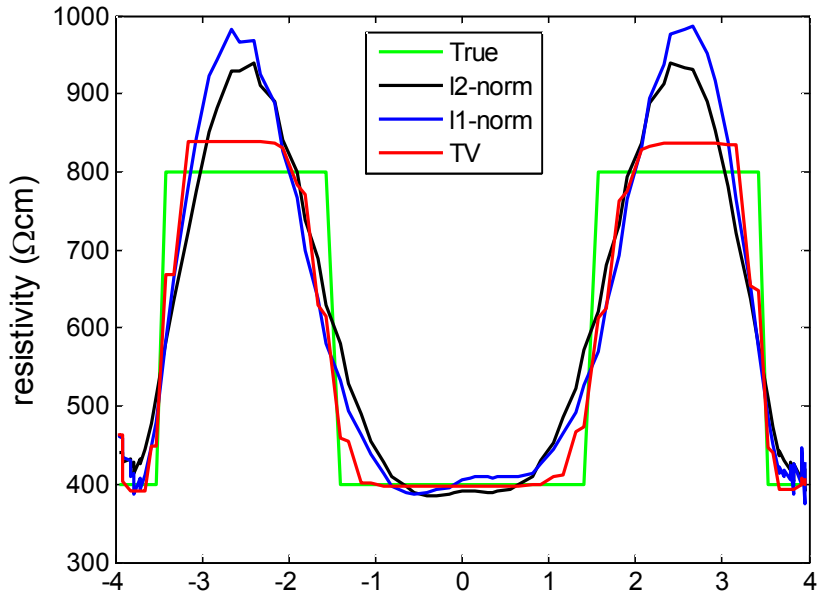

(a)

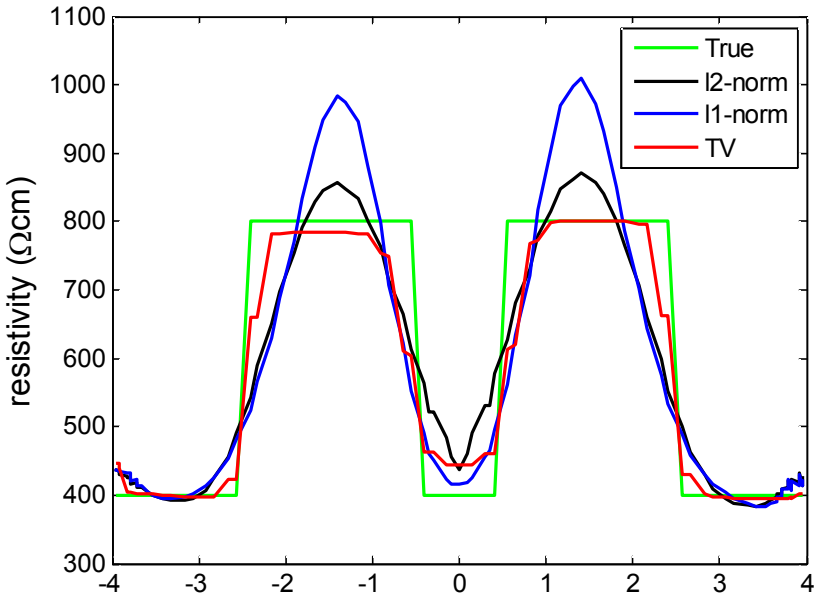

(b)

Figure 3.5. The true and estimated resistivity values along the center line without noise: (a) scenario 1 and (b) scenario 2.

(http://dx.doi.org/10.7471/ikeee.2016.20.3.226)

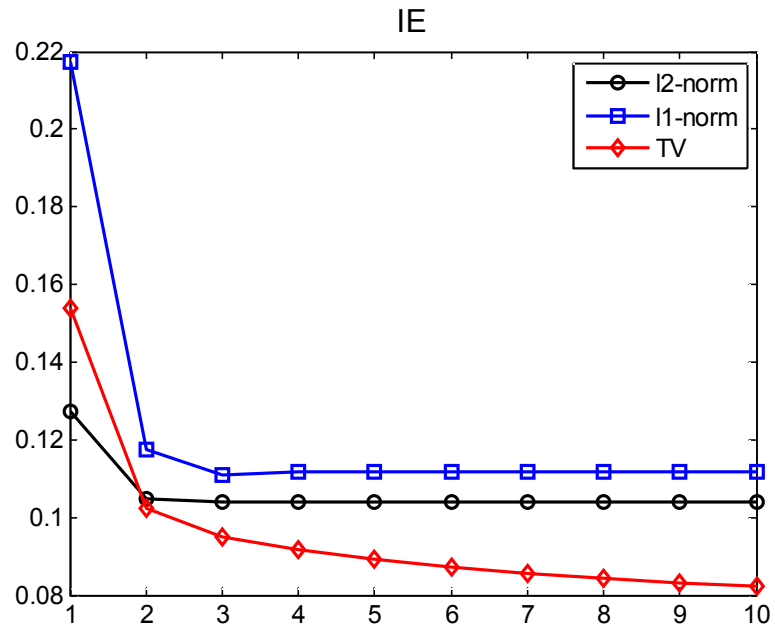

(a)

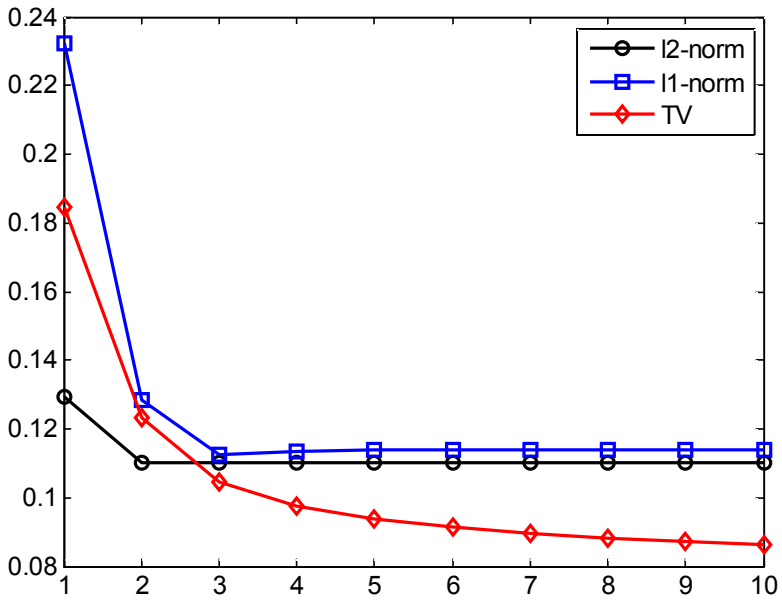

(b)

Figure 3.6. Image errors without noise: (a) scenario 1 and (b) scenario 2.

(http://dx.doi.org/10.7471/ikeee.2016.20.3.226)

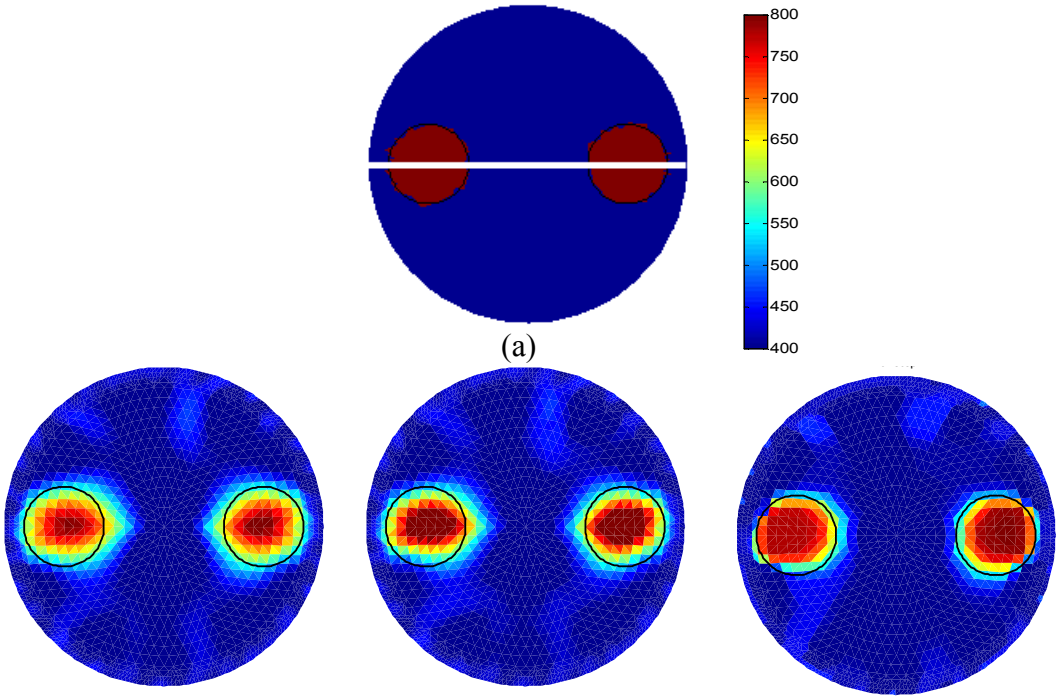

Figure 3.7. Images for scenario 1 with 1% noise: (a) true image, (b) ~ (d) the reconstructed images by the *l*2-norm, *l*1-norm, and TV regularization methods, respectively.
(http://dx.doi.org/10.7471/ikeee.2016.20.3.226)

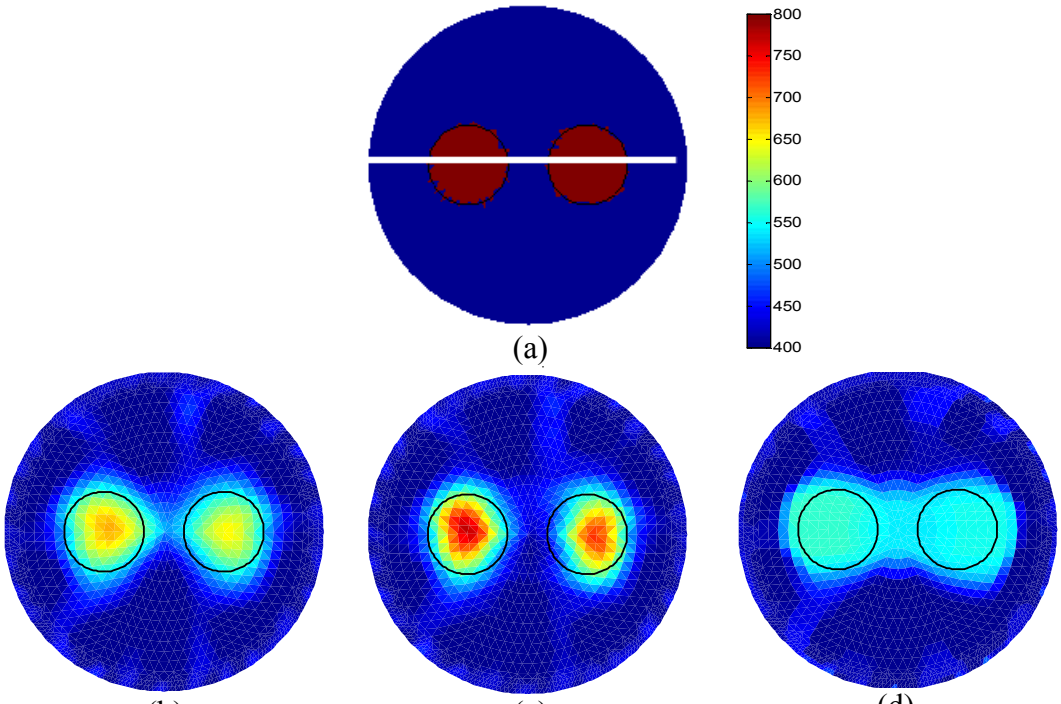

Figure 3.8. Images for the scenario 2 with 1% noise: (a) true image, (b) ~ (d) the reconstructed images by the *l*2-norm, *l*1-norm, and TV regularization methods, respectively.
(http://dx.doi.org/10.7471/ikeee.2016.20.3.226)

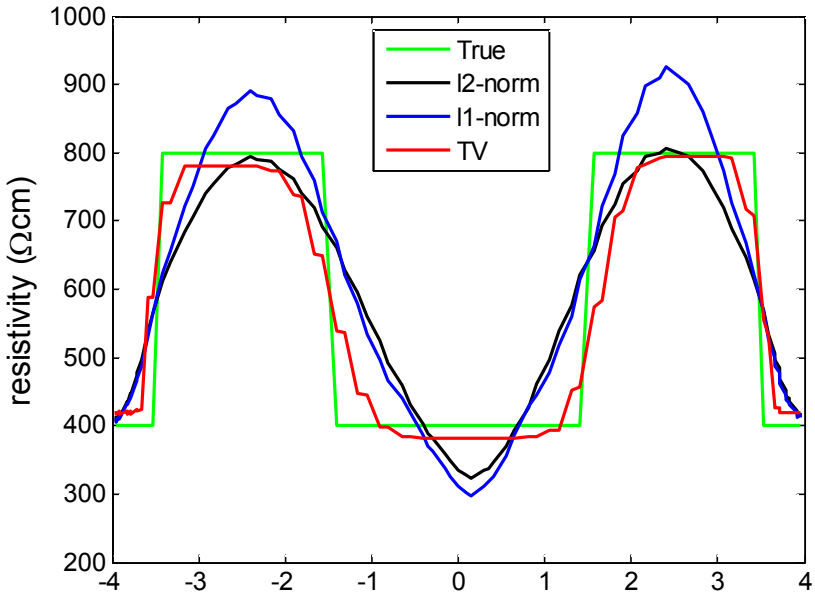

(a)

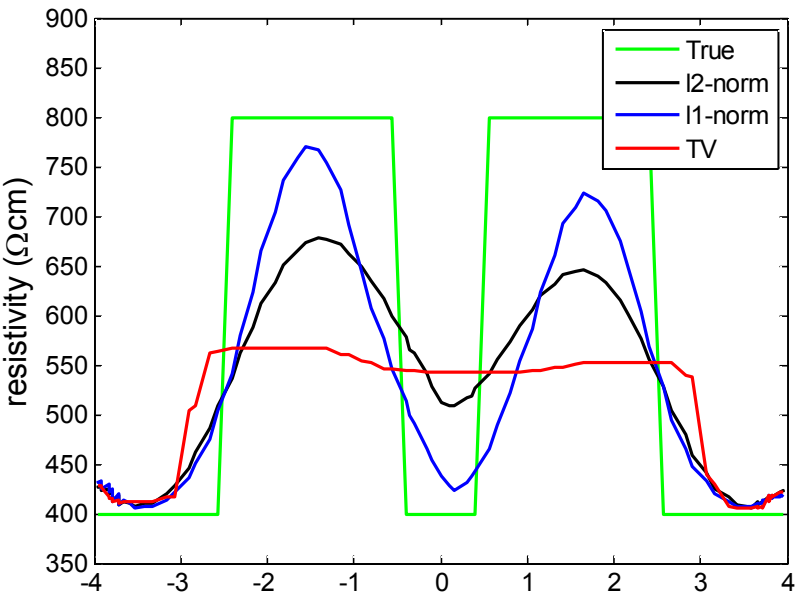

(b)

Figure 3.9. The true and estimated resistivity values along the center line with 1% noise: (a) scenario 1 and (b) scenario 2.

(http://dx.doi.org/10.7471/ikeee.2016.20.3.226)

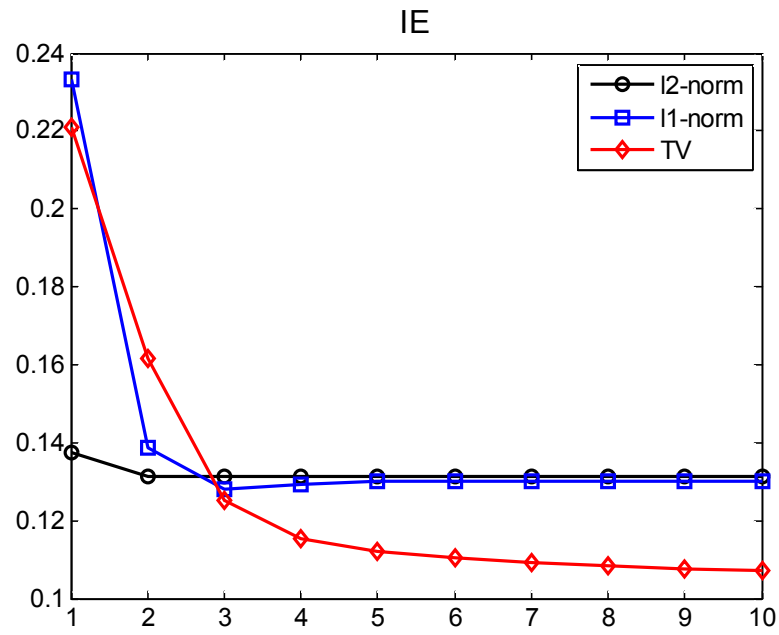

(a)

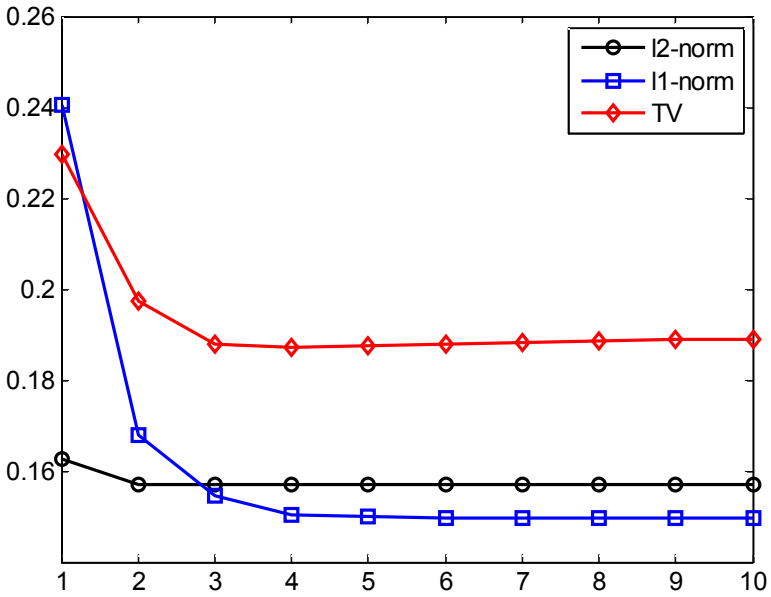

(b)

Figure 3.10. Image errors with 1% noise: (a) scenario 1 and (b) scenario 2.

(http://dx.doi.org/10.7471/ikeee.2016.20.3.226)

4. Sub-domain based Regularization Method

As mentioned earlier, the generalized Tikhonov regularization method that employs *l*2-norm regularization method uses difference-type regularization matrix as given in equation (3.17). It is commonly used method that has fast convergence and computationally efficient (Mamatjan *et al*. 2012). However, this method is difficult to recover discontinuous resistivity distribution in image reconstruction because of smoothness assumption. That is, the reconstructed images get smoothen at the boundary of internal organs or targets. The images are difficult to show the structural and functional properties caused by the differences in electrical properties inside the object.

To overcome these limitations, the *l*1-norm and TV regularization methods in chapter 3 were introduced and compared with *l*2-norm regularization method. On the other hand, as another approach in order to improve spatial resolution, the *prior* information on the internal structure of object can be incorporated into the regularization method. The *prior* information of internal structure in industrial applications can be the target's size, shape, or position and in medical applications previously available images of CT and MRI can be used. Using the *prior* information, the internal resistivity distribution can be reconstructed with sharp target boundaries and estimated more accurately.

However, for most real situations, the *prior* information on the internal structure of the whole domain cannot be known exactly. If the *prior* information on internal structure is not reliable with actual model, the reconstruction performance gets deteriorated. When partial information on the internal structure is known or available, to improve the spatial resolution in EIT a sub-domain based regularization method which is proposed in this thesis can be used.

To evaluate the performance of the sub-domain based regularization method, two applications are considered. One is human thorax monitoring and the other is two-phase flow monitoring. A part of whole domain is considered as a sub-domain, such *prior* information is incorporated into the regularization method. In the proposed regularization method, the regularization matrix is anisotropically modified to

contain *prior* information on a sub-domain. Also, the regularization parameter is set with different weight for the sub-domain.

This chapter is a reference to two papers on human thorax monitoring (Kang *et al*. 2016a) and two-phase flow monitoring (Kang *et al*. 2016b). Using the sub-domain based regularization method for human thorax monitoring is introduced in section 4.1 and two-phase flow monitoring in section 4.2.

4.1 Human thorax monitoring

4.1.1 Image reconstruction method for human thorax monitoring

Consider human thorax monitoring during cardiac cycle assuming that the lung boundaries do not change and the thorax model is simply composed of background, lungs and heart. Also, the anatomical information of human thorax can be obtained from the previous CT image of a patient. The simple thorax model in figure 4.1 can be designed by considering accurate boundaries of the lungs and an ambiguous boundary of heart during the cardiac cycle. In figure 4.1, the regions I and II correspond to background and lungs, respectively, and the region III is consist of the heart and a part of background adjoining the heart during the cardiac cycle.

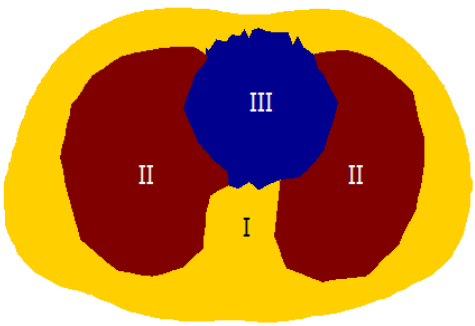

Figure 4.1. Simple thorax model with a *prior* information obtained from CT image.

(http://dx.doi.org/10.1088/0957-0233/27/2/025703)

To reconstruct the human thorax image, one-step Gauss-Newton algorithm with generalized Tikhonov regularization method is employed and can be written as

$$\hat{\rho}_1 = \rho_0 + (H^T H + \gamma \Gamma^T \Gamma)^{-1} (H^T [\tilde{U} - U(\rho_0)]). \quad (4.1)$$

The above equation (4.1) was formulated from the equation (3.13) by linearizing an initial value ρ_0 and assuming $\rho_* = \rho_0$. Here, the initial value ρ_0 generally uses the best homogeneous resistivity value.

The regularization constraint in the equation (4.1) has a quadratic form $\Gamma^T\Gamma$. The quadratic form with allocated weights in the equation (3.17) has an effect not only the neighboring elements connected to the element but also other adjacent elements connected to the neighboring elements. To easily approach a *prior* information on the internal structure for human thorax, a square matrix Γ was used instead of the quadratic form $\Gamma^T\Gamma$. Therefore, one-step Gauss-Newton method can be represented as follows

$$\hat{\rho}_1 = \hat{\rho}_0 + (H^T H + \gamma\Gamma)^{-1}(H^T[\tilde{U} - U(\hat{\rho}_0)]). \tag{4.2}$$

The generalized Tikhonov regularization method with the conventional difference matrix in equation (3.17) gives the smoothing effect in the reconstructed image since the changes in resistivity distribution inside the object are isotropic. Since this method is hard to identify the lungs and heart boundaries in human thorax, we lose important medical information from the reconstructed image. Also, with a scalar regularization parameter, it is difficult to select an optimized regularization parameter depending on the situations. A comparatively large value for the regularization parameter results in the blurred regions on the boundary of organ, whereas a smaller value produces undesirable spots in the reconstructed image

Therefore, to improve the spatial resolution of human thorax imaging, a sub-domain based regularization method with the *prior* information on internal structure is proposed. In figure 4.1, the known regions I and II can be considered as sub-domains Ω_{I} and Ω_{II} of the whole domain Ω. On the other hand, the region III belongs to the whole domain Ω. In the proposed method, to restrict the resistivity change in sub-domains within each sub-domain, the difference regularization matrix and the regularization parameter are modified.

The modified difference regularization matrix is selected in a similar way to the previous method using the *prior* information on known internal structure (Heikkinen *et al*. 2001, Kim *et al*. 2002a). However, the regularization matrix in the proposed

method is different from the previous methods that consider the known internal structure from the whole domain as to be separate. In the proposed method, the regularization matrix is constructed to consider the partially known internal structure as sub-domains.

Figure 4.2 describes *i* th row and *j* th row of the difference matrix for three different methods. Figure 4.2(a) shows the conventional method in the equation (3.17) that does not consider any *prior* information of known internal structure. Figure 4.2(b) shows the previous method with known internal structure, i.e. region II. Figure 4.2(c) shows the proposed method employing the sub-domain principle.

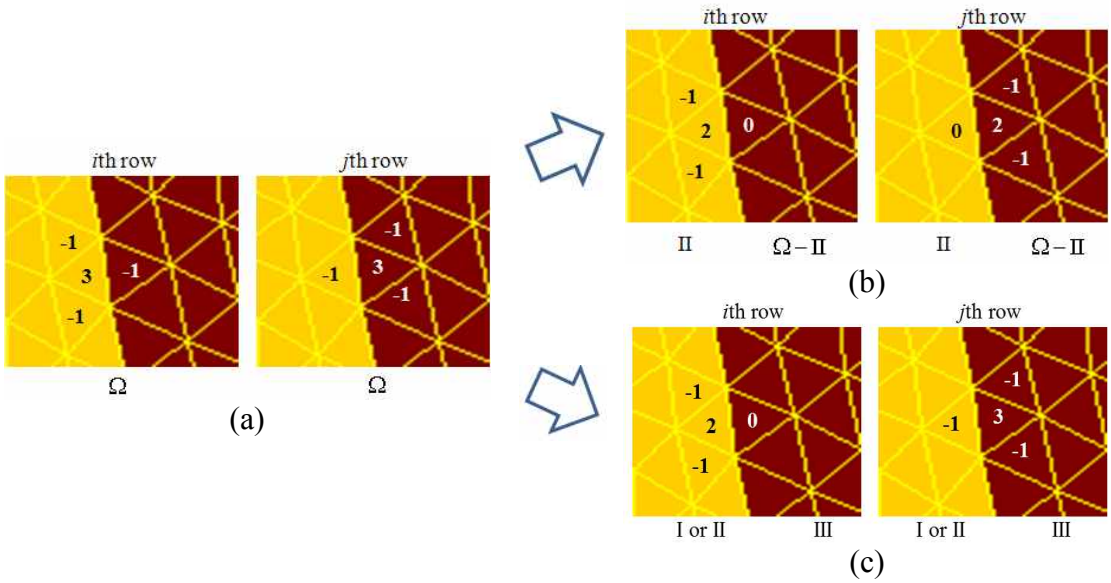

Figure 4.2. The diagram for the difference regularization matrix in: (a) conventional method, (b) previous method with known internal structure, and (c) proposed method employing sub-domain principle.

(http://dx.doi.org/10.1088/0957-0233/27/2/025703)

In figure 4.2(b), the elements on the boundary of the known internal structure are treated in the manner as the domain boundary in the equation (3.18). In this method, since the heart boundary during the cardiac cycle is not known, only region II is the known internal structure. The difference matrix is modified for the row vectors corresponding to all inner and outer elements on the boundary of region II as shown in figure 4.2(b). Using this approach, region II is treated as separate from the whole domain Ω. Just using known lung structure does not give desired performance. The region II appears discretely in the reconstructed image, but regions I and III get

smoothen. If we consider the known internal structure as regions I and II, the reconstructed images get smoothen inside each region, and we cannot obtain the meaningful image about heart boundary during the cardiac cycle.

On the other hand, in figure 4.2(c), the difference matrix is modified for the row vectors corresponding to the only inner elements on the boundary of sub-domains Ω_{I} or Ω_{II}. The row vectors for the outer elements on the boundary of sub-domains are handled in the same way as the conventional method. With this, the resistivity changes in the sub-domains have an effect on the resistivity changes within each sub-domain, however, the resistivity changes in region III are affected by the resistivity changes in the whole domain. If i th element is the inner element on the boundary of sub-domains and has one outer adjacent element, i th row of new difference matrix Γ^* can be written as follows

$$\Gamma_i^* = [0,\cdots,0,-1,0,\cdots,0,-1,0,\cdots,0,2,0,\cdots,0,0,0,\cdots,0], \tag{4.3}$$

where the column of the outer adjacent element is allocated as 0 and the column of i th element is replaced by 2 which is the absolute sum value of two inner elements. It should be noticed that the new regularization matrix Γ^* is not a symmetric matrix. The new regularization matrix Γ^* is written as follows

$$\Gamma^* = \Gamma_{\mathrm{I}}^* + \Gamma_{\mathrm{II}}^* + \Gamma_{\mathrm{III}}^*, \tag{4.4}$$

where Γ_{I}^*, Γ_{II}^* and $\Gamma_{\mathrm{III}}^* \in R^{N_e \times N_e}$ are composed of the corresponding row sets of regions I, II and III, respectively and the others as zero rows. This sub-domain approach can provide different weights for each region in regularization parameter. The Γ_{I}^*, Γ_{II}^* and Γ_{III}^* in the equation (4.4) are weighted with γ_1 , γ_2 and γ_3 respectively.

Therefore, the one-step Gauss-Newton algorithm with the proposed regularization method can be written as

$$\hat{\rho}_1 = \hat{\rho}_0 + (H^T H + \gamma_1 \Gamma_{\mathrm{I}}^* + \gamma_2 \Gamma_{\mathrm{II}}^* + \gamma_3 \Gamma_{\mathrm{III}}^*)^{-1}(H^T[\tilde{U} - U(\hat{\rho}_0)]). \tag{4.5}$$

Here, γ_1 and γ_2 are set to higher value than γ_3 because they penalize the regions I and II which can be considered to have a single resistivity distribution in each region. However, γ_3 should be set to a value as small as possible because it regularizes to distinguish heart from background. Here, γ_3 is the equal to γ in the equation (4.2).

4.1.2 Numerical simulations and phantom experiments

Computer simulations with synthetic data and experimental data are performed to investigate the performance of a sub-domain based regularization method on the spatial resolution for human thorax monitoring. To monitor human thorax while the patient holds his breath for the heart diagnosis, the resistivity of heart and lungs is assumed to be constant during the cardiac cycle. The heart expands and contracts during the cardiac cycle, so, the size and resistivity of heart change. However, since the average resistivity of heart does not have large variation, the resistivity of heart is considered as constant.

One-step Gauss-Newton algorithm is used and compared with three different regularization methods named conventional regularization method (CRM) in equation (4.2), proposed regularization method (PRM1) with constant regularization parameter ($\gamma_1 = \gamma_2 = \gamma_3$) in the equation (4.5), and proposed regularized method (PRM2) with different weights for each sub-domain.

In figure 4.3, FEM mesh for human thorax imaging with exact lung structure is considered. Also, two different meshes are used to avoid inverse crime. Fine mesh in figure 4.3(a) consists of 3028 triangular elements and 1637 nodes, and coarse mesh in figure 4.3(b) is composed of 2216 triangular elements and 1230 nodes. Fine mesh is used to generate the synthetic voltage data for numerical simulation and estimate the resistivity distribution for experiments. Coarse mesh is used to estimate the resistivity distribution for numerical simulation. An array of 16 electrodes is attached on the surface of the thorax. The adjacent current patterns are used, and the voltage data is measured on the surface of all 16 electrodes.

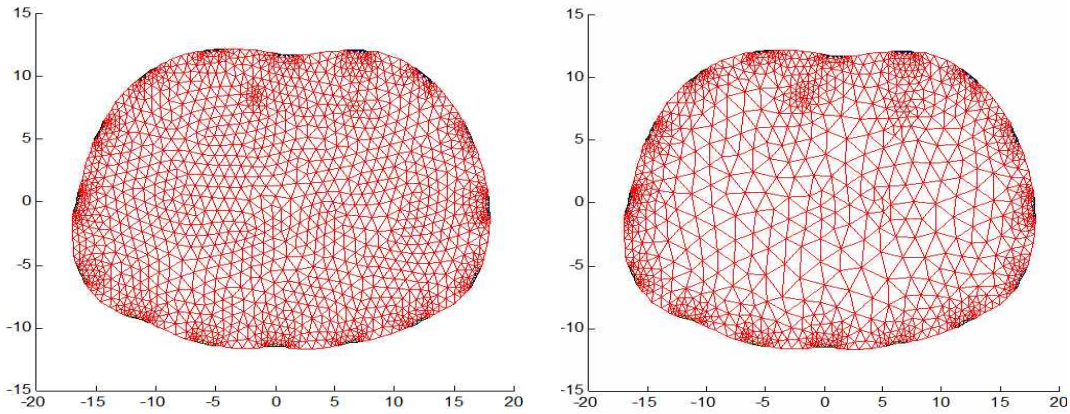

(a) (b)

Figure 4.3. Meshes for 2D thorax model: (a) fine mesh and (b) coarse mesh.

(http://dx.doi.org/10.1088/0957-0233/27/2/025703)

Two different sizes of heart corresponding to systole (small heart) and diastole (big heart) are considered. The resistivity of background, lungs, and heart are set to 495 Ωcm , 645 Ωcm and 207 Ωcm , respectively (Bruder *et al.* 1994, Vauhkonen 1997, Baysal and Eyuboglu 2000, Rashid *et al.* 2011), and these values can be acceptable clinically.

Synthetic and experimental voltage data $\tilde{U}_{\mathrm{h}}$ with homogeneous background resistivity instead of $U(\rho_0)$ are used in computing the equations (4.2) and (4.5). This approach can minimize the modeling errors related to truncation of the computational domain, electrode position, contact impedance, and etc.

In the numerical simulations, $\hat{\rho}_0$ is calculated as 497 Ωcm and 491 Ωcm for the small and big heart cases, respectively. In the experimental studies, $\hat{\rho}_0$ is calculated as 505 Ωcm and 497 Ωcm for the small and big heart cases, respectively.

For the numerical simulations, the regularization parameter γ in CRM and γ_1, γ_2 , and γ_3 in PRM1 are set to 5×10^{-4} ($\gamma_1=\gamma_2=\gamma_3$). In PRM2, γ_3 is equal to γ , and γ_1, γ_2 are set to 5×10^{-2} that is weighted 100 times more than γ . For the experimental studies, the regularization parameter γ in CRM and γ_1, γ_2 , and γ_3 in PRM1 are set to 10^{-4} . In PRM2, γ_3 is equal to γ , and γ_1 and γ_2 are set to 10^{-2} that is weighted 100 times more than γ .

■ **Experimental setup**

For the experiments, as a current source, agilent 4284A LCR meter is used and NI PXIe-1062Q is used to acquire voltages. The experimental phantom has the same geometry as in figure 4.3. Electrodes with height of 5 cm and width of 1.8 cm are attached around the phantom periphery. The experimental phantom is filled with saline solution that has resistivity of 495 Ωcm up to the depth of the electrode to simulate two-dimensional conditions. The lungs and heart are made of agar with mean resistivity of approximately 645 Ωcm and 207 Ωcm, respectively.

■ **Performance evaluation index**

In numerical simulations, to compare the estimation performance, the image error (IE) in the equation (3.30) and the correlation coefficient (CC) between true resistivity and estimated resistivity are used. The CC is defined as follows

$$\mathrm{CC} = \frac{\sum_{i=1}^{N_e}[(\rho_i - \bar{\rho})(\hat{\rho}_i - \bar{\hat{\rho}})]}{\sqrt{\sum_{i=1}^{N_e}(\rho_i - \bar{\rho})^2 \sum_{i=1}^{N_e}(\hat{\rho}_i - \bar{\hat{\rho}})^2}}, \tag{4.6}$$

where $\bar{\rho}$, $\bar{\hat{\rho}}$ are the mean values of the true resistivity distribution ρ and the estimated resistivity distribution $\hat{\rho}$, respectively. It should be noticed that the bigger CC value and smaller IE value correspond to better reconstruction performance.

(a) Numerical results and discussion

Figures 4.4 and 4.5 show the true and reconstructed images for the small and big heart cases using synthetic data. The true resistivity distribution is given in figures 4.4(a) and 4.5(a). The reconstructed images by CRM, PRM1 and PRM2 for small heart case are shown in figures 4.4(b-d) and for big heart cases are shown in figure 4.5(b-d), respectively. The color bar for all the images is shown in same scale (200 to 650 Ωcm).

In figures 4.4(b) and 4.5(b), the images using CRM without known structure information has the poorest spatial resolution with non-uniform background with unclear lung boundaries as compared to the other methods. In figures 4.4(c) and

4.5(c), with PRM1, the spatial resolution is slightly improved and has sharp edges of lungs compared to CRM but still the resistivity distribution is not estimated well. The results using PRM2 in figures 4.4(d) and 4.5(d) have clear background and lungs, and the heart size and position are close to true images. The improvement in the resolution of background and lungs makes the heart appear more distinctly. Moreover, the size and location of heart are estimated with better accuracy by using PRM2.

Figure 4.6 shows the sorted resistivity distributions for the numerical simulations. As noticed in figures 4.4 and 4.5, PRM2 has more uniform resistivity distribution in background and lungs and fast transient at the boundaries of the heart and lungs compared to the CRM and PRM1. That is, the results mean that PRM2 has more uniform resistivity distribution in sub-domains and more discrete changes on the organ boundary as shown in figures 4.4 and 4.5.

Table 4.1 shows IE and CC results for numerical simulations to evaluate the reconstruction performance of CRM, PRM1 and PRM2. It can be noticed that PRM2 has the lowest IE and highest CC values compared to the other methods.

Table 4.1. IE and CC results for numerical simulations

Index	IE			CC		
	CRM	PRM1	PRM2	CRM	PRM1	PRM2
Small heart	0.0806	0.0543	0.0444	0.7722	0.9039	0.9358
Big heart	0.1032	0.0735	0.0550	0.7667	0.8880	0.9380

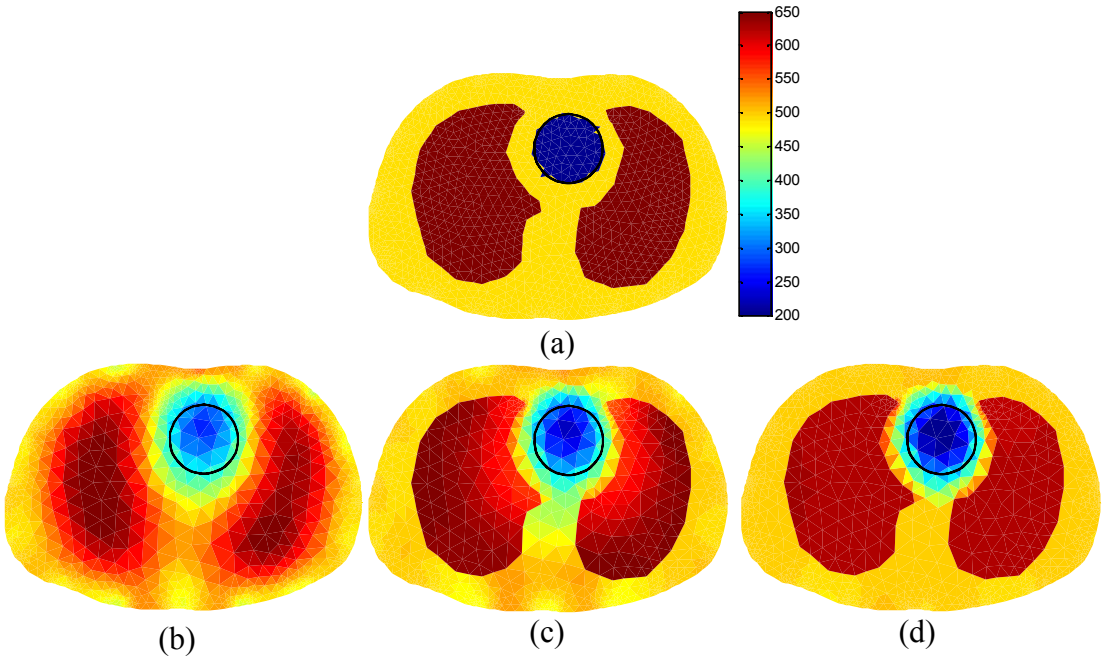

Figure 4.4. Images for the small heart case using synthetic data: (a) true image, (b) image by CRM, (c) image by PRM1, and (d) image by PRM2. The black circle in the images represents the true position of heart.

(http://dx.doi.org/10.1088/0957-0233/27/2/025703)

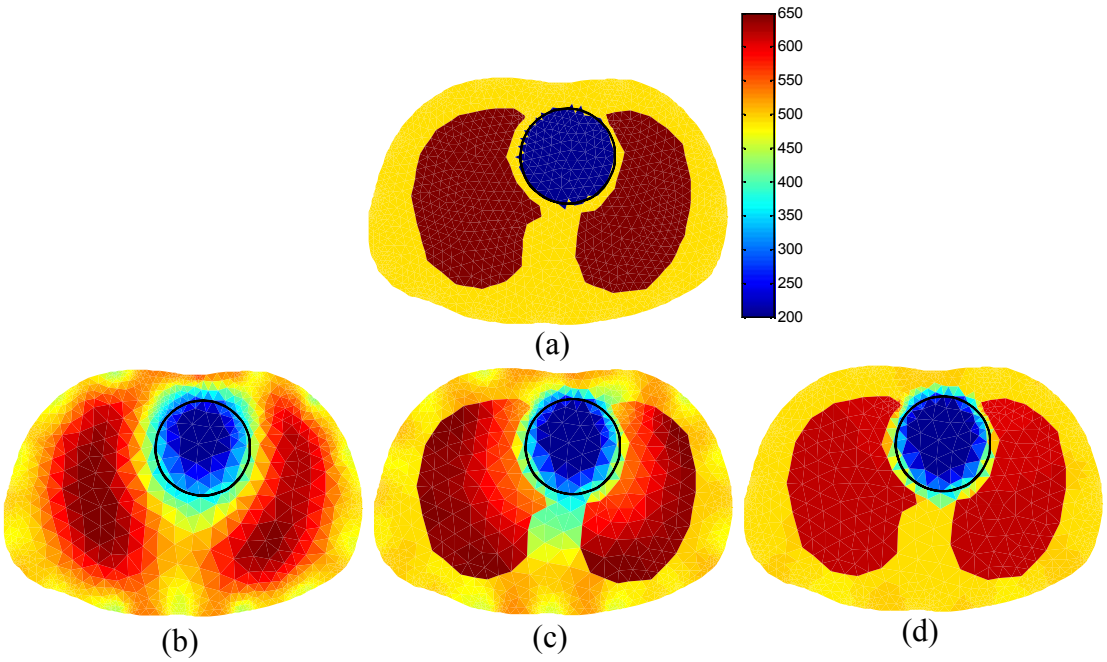

Figure 4.5. Images for the big heart case using synthetic data: (a) true image, (b) image by CRM, (c) image by PRM1, and (d) image by PRM2. The black circle in the images represents the true position of heart.

(http://dx.doi.org/10.1088/0957-0233/27/2/025703)

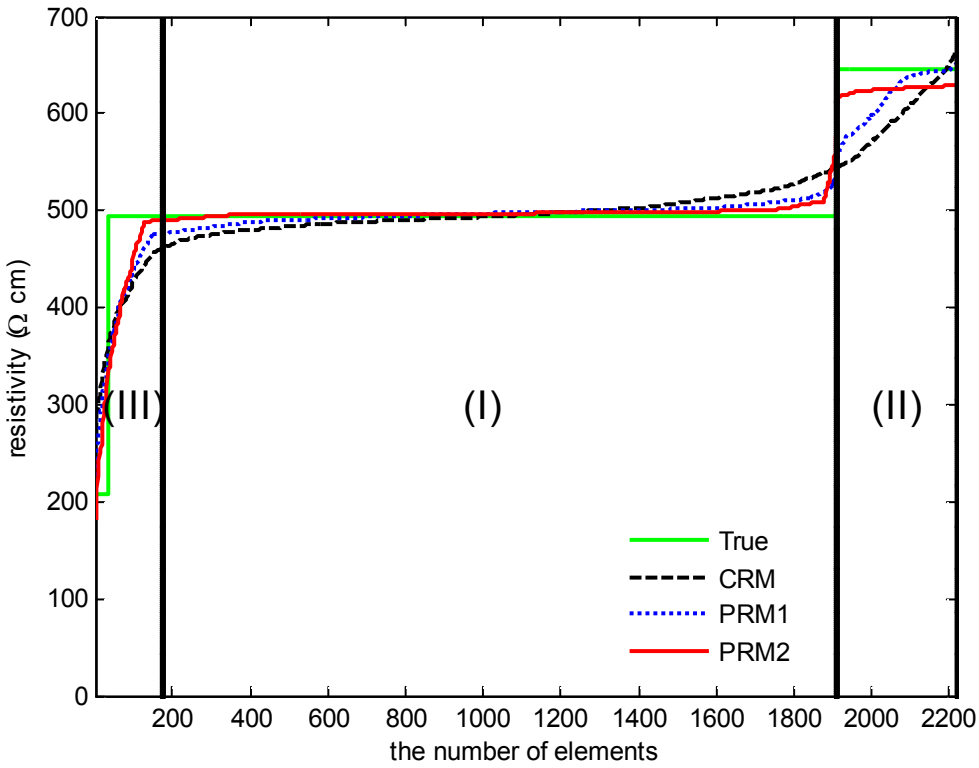

(a)

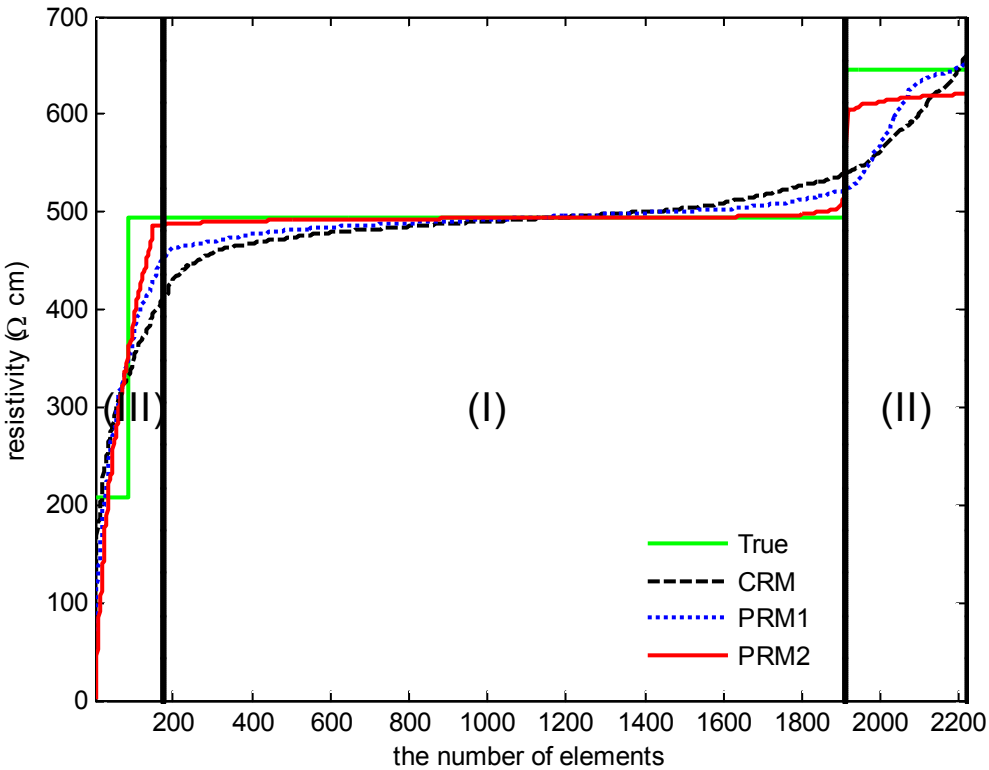

(b)

Figure 4.6. The sorted resistivity distributions for numerical cases: (a) small heart and (b) big heart.

(http://dx.doi.org/10.1088/0957-0233/27/2/025703)

(b) Experimental results and discussion

Figures 4.7 and 4.8 show the true and reconstructed images for the small heart case and the big heart case using experimental data. The true images are shown in figures 4.7(a) 4.8(a). The reconstructed images by CRM, PRM1 and PRM2 for small heart case are shown in figures 4.7(b-d) and for large heart case are shown in figures 4.8(b-d), respectively.

In figures 4.7(b) and 4.8(b) by using CRM, the spatial resolution is poor due to the smoothened regions surrounding the organ boundaries. Also, the heart size is over estimated compared to the heart size in true image. In figures 4.7(c) and 4.8(c), PRM1 gives a better spatial resolution compared to CRM because it regulates the variation in resistivity distribution within the each sub-domain for lungs and background. However, the region in between lungs is still ambiguous. In figures 4.7(d) and 4.8(d) by using PRM2 with different weights of each sub-domain, the spatial resolution is improved compared to the CRM and PRM1. The different weight makes spatial resolution of the background and lung regions more clear, thus the heart size and position are estimated more accurately.

Figure 4.9 shows the sorted resistivity distributions for the experimental simulations. As noticed in figure 4.9, PRM2 has more uniform resistivity distribution in sub-domains and more fast transient at the organ boundary compared to the CRM and PRM1, as shown in the results of numerical simulations.

Consequently, all the results for the numerical and experimental simulations show that PRM has improved resolution compared to CRM.

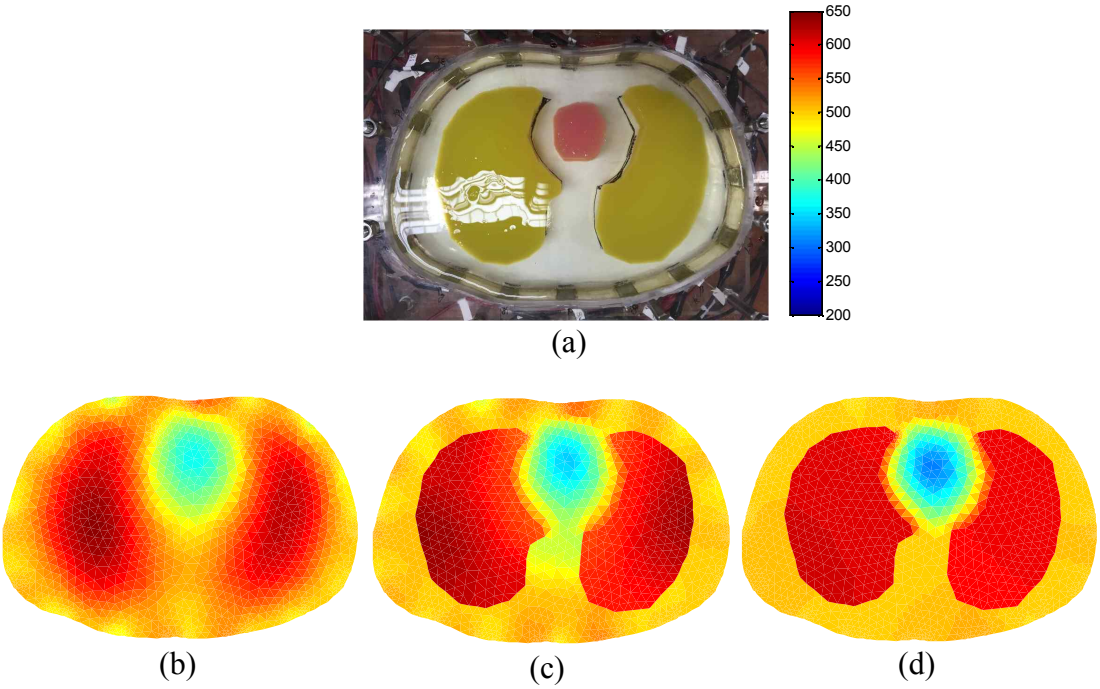

Figure 4.7. Images for the small heart case using experimental data: (a) true image, (b) image by CRM, (c) image by PRM1, and (d) image by PRM2

(http://dx.doi.org/10.1088/0957-0233/27/2/025703)

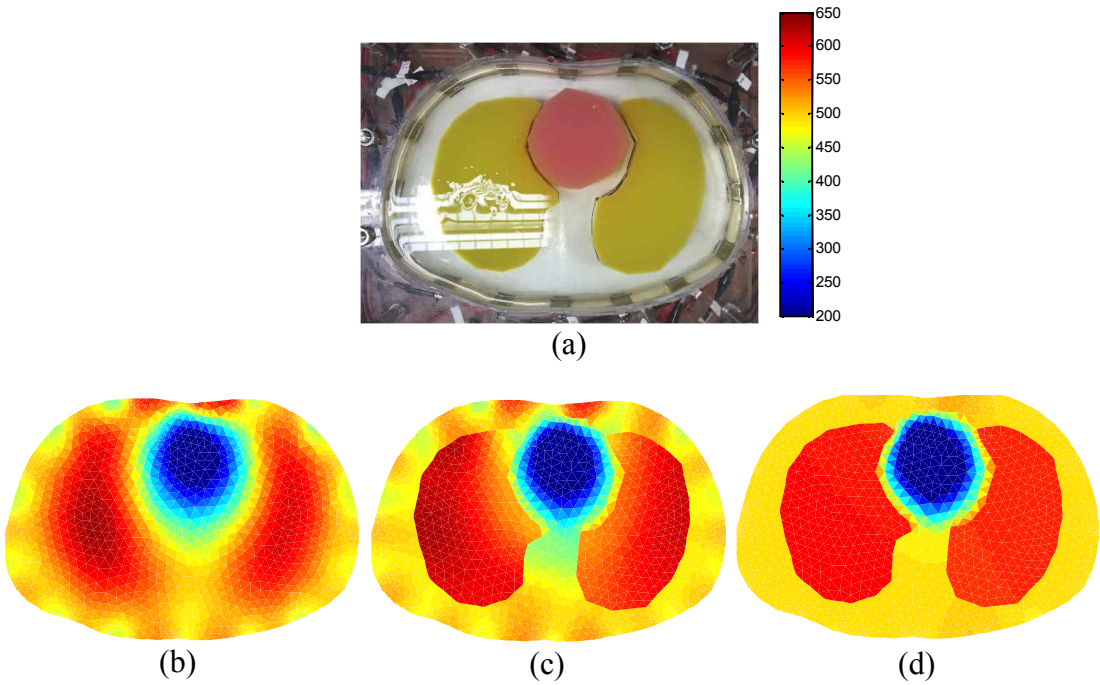

Figure 4.8. Images for the big heart case using experimental data: (a) true image, (b) image by CRM, (c) image by PRM1, and (d) image by PRM2.

(http://dx.doi.org/10.1088/0957-0233/27/2/025703)

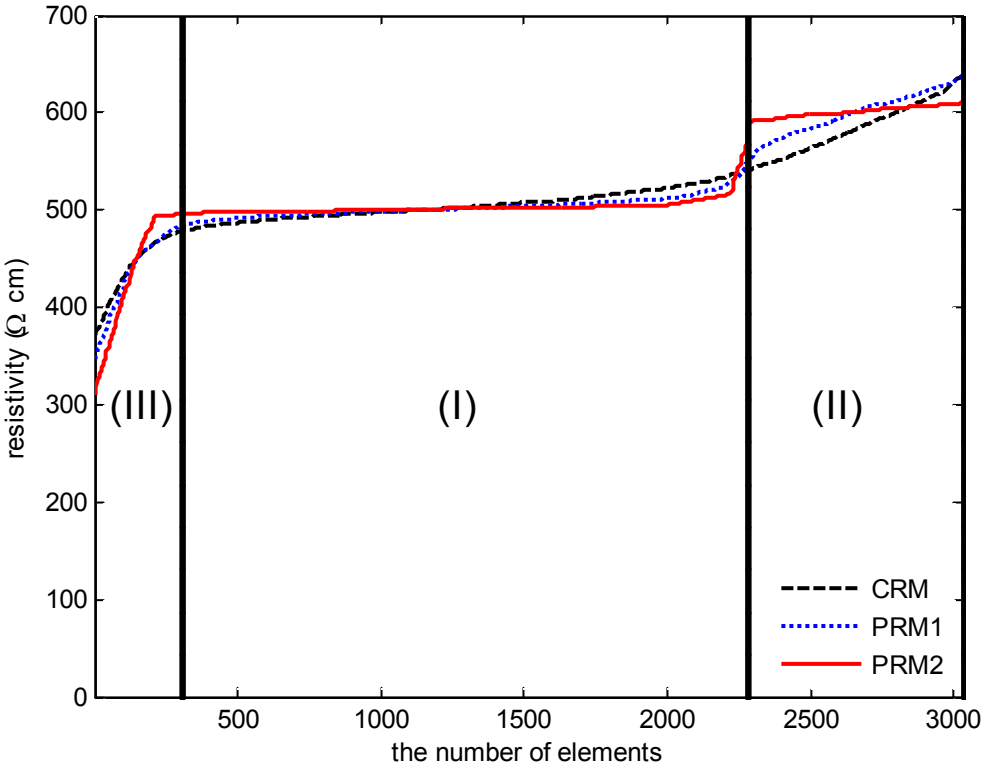

(a)

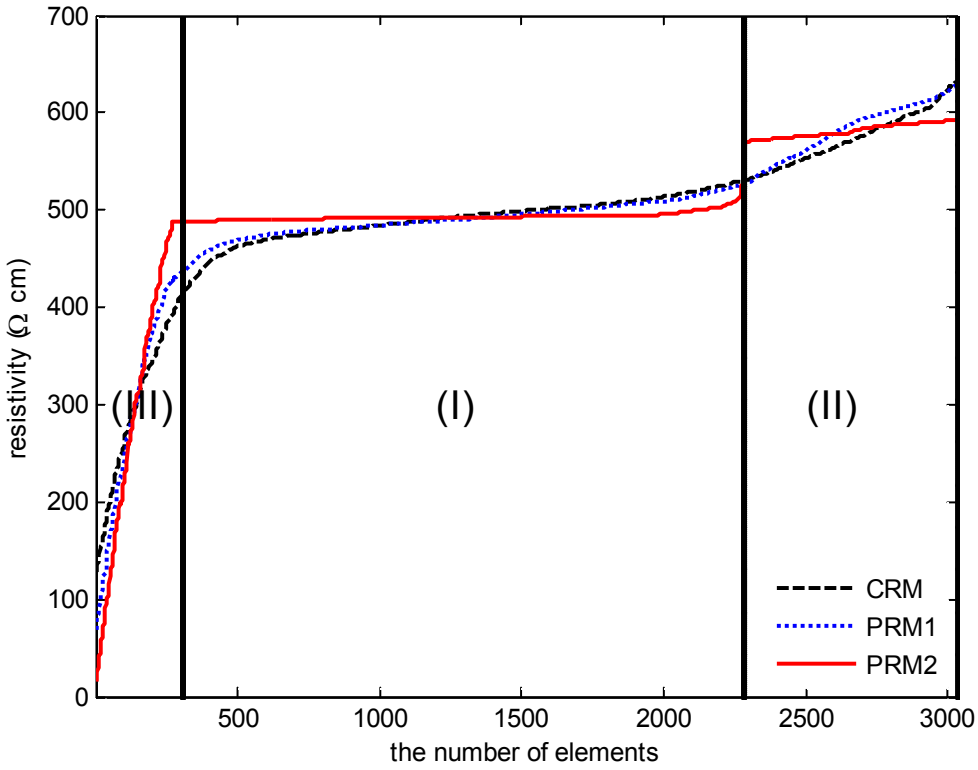

(b)

Figure 4.9. The sorted resistivity distributions for experimental cases: (a) small heart and (b) big heart.

(http://dx.doi.org/10.1088/0957-0233/27/2/025703)

4.2 Two-phase flow monitoring

Two-phase flow phenomena are frequently encountered in many engineering applications, such as heat exchanger, oil or natural gas pumping system, and nuclear power plant. For example, the bubbles with high resistivity are formed within liquid contained in a pipe. Since this two-phase phenomenon can reduce process efficiency and disturb safe operations, the two-phase flow system is monitored. In this section in order to improve the spatial resolution of two-phase flow image, a sub-domain based regularization method is applied.

4.2.1 Image reconstruction method for two-phase flow monitoring

In two-phase flow monitoring, to obtain a sub-domain as a *prior* information on the internal structure, Otsu's thresholding method (Otsu 1979) is used after 1st iteration of iterative Gauss-Newton algorithm in the equation (3.14). The background classified using Otsu' thresholding method is considered as a sub-domain.

The iterative Gauss-Newton algorithm with the *l*2-norm regularization in the equation (3.14) is rewritten as

$$\hat{\rho}_{i+1} = \hat{\rho}_i + (H_i^T H_i + \gamma\Gamma^T\Gamma)^{-1}\{H_i^T[\tilde{U} - U(\hat{\rho}_i)] - \gamma\Gamma^T\Gamma\hat{\rho}_i\}. \tag{4.7}$$

Using the sub-domain based regularization method, the above equation is modified as

$$\hat{\rho}_{i+1} = \hat{\rho}_i + [J^T J + (\varsigma\Gamma^*)^T\Gamma^*]^{-1}\{J^T[V - U(\hat{\rho}_i)] - (\varsigma\Gamma^*)^T\Gamma^*\hat{\rho}_i\}, \tag{4.8}$$

where Γ^* is the new regularization matrix considered the sub-domain, ς is the regularization parameter. The procedure of the proposed method is described in the following steps.

Procedure of the proposed method

1. Find an initial guess $\hat{\rho}_0$ and compute the $U(\hat{\rho}_0)$ and $J(\hat{\rho}_0)$.
2. Update $\hat{\rho}_1$ by using the equation (4.7).
3. Identify the FEM elements that belong to a sub-domain Ω_{BG} from a whole domain by using Otsu's thresholding method.
4. Obtain the new regularization matrix Γ^*.
5. Set γ_1 for the sub-domain to a higher value than γ_2 that is equal to γ.
6. Update the resistivity distribution by using the equation (4.8) after 1st iteration of Gauss-Newton algorithm.

Let's consider the suitable sub-domain selected by Otsu's thresholding method. The sub-domain can be considered to be composed of background, but it isn't exactly same to actual background. The other region except for the sub-domain regions is considered to be composed of target and the other background.

As mentioned in the section 4.1, if the proper sub-domain is selected, the new regularization matrix Γ^* is obtained from Γ considering the sub-domain. If the k th element belongs to inner elements on the boundary of the sub-domain Ω_{BG}, Γ_k^* is modified from Γ_k in the equation (3.17) by removing the column weight -1 s of the outer adjacent elements corresponding to the inner elements. In that case, the number 3 is replaced by 2, i.e., the absolute sum value of two inner element weights. The whole domain Ω can include the sub-domain by modifying only row vectors of inner elements on the boundary of the sub-domain Ω_{BG}. The new regularization matrix Γ^* is not a symmetric matrix, and it can be partitioned by rows as

$$\Gamma^* = \begin{bmatrix} \Gamma_1^* \\ \Gamma_2^* \\ \vdots \\ \Gamma_{N_e}^* \end{bmatrix}, \qquad \Gamma_k^* \equiv \left\{ \Gamma_{k1}^* \;\; \Gamma_{k2}^* \;\; \cdots \Gamma_{kN_e}^* \right\}. \tag{4.9}$$

The regularization parameter ς is set with different weights for the each Γ_k^*, as follows

$$\varsigma_k = \begin{cases} \gamma_1, & k \in \text{elements in } \Omega_{\text{BG}} \\ \gamma_2, & k \in \text{otherwise} \end{cases} \tag{4.10}$$

where γ_1 for the elements in Ω_{BG} is set to be a more weighted value than γ_2 for the other elements because it penalizes the sub-domain Ω_{BG} which can be considered to have a single resistivity distribution, however, γ_2 is set to the value as small as possible because it regularizes to distinguish actual targets from background. Here, γ_2 is identical to γ in the equation (4.7).

4.2.2 Selecting a sub-domain by Otsu's thresholding method

Otsu's thresholding method is described to select a sub-domain. The Otsu's thresholding method is commonly used to select a proper threshold for distinguishing targets from its background in a given image.

Let the FEM elements of the reconstructed image be represented in gray levels $\{1,2,\cdots,t,\cdots,T\}$, and suppose that the reconstructed image be divided into two classes A and B by a threshold at level t. The class A represents elements with levels from 1 to t, and Class B represents elements with levels from $t+1$ to T. The number of elements at level j is represented by o_j and the total number of elements is represented by $N_e = o_1 + o_2 + \ldots + o_T$.

The gray level histogram is normalized and considered as a probability distribution as follows

$$p_j = o_j / N_e, \quad p_j \geq 0, \quad \sum_{j=1}^{T} p_j = 1. \tag{4.11}$$

Then, the probabilities of each class occurrence are given by

$$\omega_A \equiv \omega_A(t) = \sum_{j=1}^{t} p_j = \omega(t), \tag{4.12}$$

$$\omega_B \equiv \omega_B(t) = \sum_{j=t+1}^{T} p_j = 1 - \omega_A = 1 - \omega(t), \tag{4.13}$$

where $\omega(t) \equiv \sum_{j=1}^{t} p_j$ is the zeroth order cumulative moments of histogram.

The each class mean level is given by

$$\mu_A \equiv \mu_A(t) = \frac{1}{\omega_A} \sum_{j=1}^{t} jp_j = \frac{\mu(t)}{\omega(t)}, \tag{4.14}$$

$$\mu_B \equiv \mu_B(t) = \frac{1}{\omega_B} \sum_{j=t+1}^{T} jp_j = \frac{\mu_T - \mu(t)}{1 - \omega(t)}, \tag{4.15}$$

where $\mu(t) \equiv \sum_{j=1}^{t} jp_j$ is the first order cumulative moments of histogram, and the total mean level is given by

$$\mu_T \equiv \mu(T) = \sum_{j=1}^{T} jp_j = \omega_A \mu_A + \omega_B \mu_B. \tag{4.16}$$

The each class variance is given by

$$\sigma_A^2 \equiv \sigma_A^2(t) = \frac{1}{\omega_A} \sum_{j=1}^{t} (j - \mu_A)^2 p_j, \tag{4.17}$$

$$\sigma_B^2 \equiv \sigma_B^2(t) = \frac{1}{\omega_B} \sum_{j=t+1}^{T} (j - \mu_B)^2 p_j. \tag{4.18}$$

Otsu's thresholding method seeks for the optimal threshold that minimizes the within-class variance, or equivalently maximizes between-class variance. The within-class variance and the between-class variance, respectively, are defined as

$$\sigma_{within}^2(t) = \omega_A \sigma_A^2 + \omega_B \sigma_B^2, \tag{4.19}$$

$$\sigma_{between}^2 = \omega_A (\mu_A - \mu_T)^2 + \omega_B (\mu_B - \mu_T)^2, \tag{4.20}$$

and the total variance of levels is

$$\sigma_T^2 = \sum_{j=1}^{T} (j - \mu_T)^2 p_j. \tag{4.21}$$

Using equations (4.14) ~ (4.16) and $\omega_A + \omega_B = 1$, the between-class variance can be rewritten as

$$\begin{aligned} \sigma_{between}^2 &= \omega_A(\mu_A - \mu_T)^2 + \omega_B(\mu_B - \mu_T)^2 \\ &= \omega_A\omega_B(\mu_B - \mu_A)^2 \\ &= \omega(t)\left[1 - \omega(t)\right]\left[\frac{\mu_T - \mu(t)}{1 - \omega(t)} - \frac{\mu(t)}{\omega(t)}\right]^2 \\ &= \frac{[\mu_T\omega(t) - \mu(t)]^2}{\omega(t)[1 - \omega(t)]}, \end{aligned} \tag{4.22}$$

The optimal threshold t^* is obtained by

$$t^* = \arg\max_{1 \le t < T} \sigma_{between}^2(t). \tag{4.23}$$

4.2.3. Numerical simulations and phantom experiments

The reconstruction performance of the sub-domain regularization method for the two-phase flow monitoring is evaluated by performing numerical and experimental simulations. In the numerical and experimental simulations, an industrial pipe with a radius of 4 cm is considered. Also, four cases with two or more bubbles appearing within the homogeneous liquid inside the flow domain are tested. To carry out the computer simulations, two mesh structures in figure 3.2 are used. Also, 32 electrodes with a width of 0.6 cm are used. Synthetic data for numerical simulations are generated using an unstructured mesh in figure 3.2(a). The resistivity distribution for both numerical simulations and experimental simulation is estimated using a structured mesh in figure 3.2(b).

To perform numerical simulations, the background is considered to be liquid with a resistivity value of 300 Ωcm and the targets are considered to be void or bubbles with a high resistivity value of 2000 Ωcm. The 1% relative white Gaussian noise of synthetic voltage data is added to the synthetic voltage to represent the real situations. The added noise corresponds to the instrument handling, environmental conditions and numerical error of FEM mesh.

The reconstructed images of numerical and experimental cases are compared using iterative Gauss-Newton algorithm with the conventional regularization method (CRM) in the equation (4.7) and the proposed sub-domain based regularization method (PRM) in the equation (4.8). They are also compared with the *l*1-norm regularization method (*l*1-norm) in the equation (3.22) and TV regularization method (TV) in the equation (3.28) developed for non-smooth images. Trigonometric current patterns are injected through the electrodes and the corresponding voltages are measured on all electrodes.

In the numerical simulations, the values of regularization parameter for CRM, *l*1-norm and TV in table 4.2 are the optimized values which correspond to low image error. In the experimental simulations, the values of regularization parameter for CRM and *l*1-norm and TV which are shown in table 4.3 are chosen a *posteriori* by visual inspection. In PRM, γ_2 is equal to the value γ, and γ_1 is set to a value weighted 100 times more than γ_2 to constrain a sub-domain Ω_{BG}. In the *l*1-norm and TV regularization method, the small positive value δ is set to 10^{-6}.

Table 4.2. The values of regularization parameter for numerical simulations with 1% noise

Index	CRM(γ)	*l*1-norm(γ)	TV (γ)	PRM(γ_1, γ_2)
Case 1	5×10^{-4}	5×10^{-1}	5×10^{-2}	5×10^{-2}, 5×10^{-4}
Case 2	10^{-3}	5×10^{-1}	10^{-1}	10^{-1}, 10^{-3}
Case 3	5×10^{-4}	10^{-1}	10^{-1}	5×10^{-2}, 5×10^{-4}
Case 4	5×10^{-4}	10^{-1}	5×10^{-2}	5×10^{-2}, 5×10^{-4}

(http://dx.doi.org/10.1016/j.flowmeasinst.2016.06.002)

Table 4.3. The values of regularization parameter for experimental simulations

Index	CRM(γ)	*l*1-norm(γ)	TV(γ)	PRM(γ_1, γ_2)
Case 1	5×10^{-4}	10^{-1}	5×10^{-3}	5×10^{-2}, 5×10^{-4}
Case 2	10^{-3}	5×10^{-1}	10^{-2}	10^{-1}, 10^{-3}
Case 3	5×10^{-3}	5×10^{-1}	15	5×10^{-1}, 5×10^{-3}
Case 4	5×10^{-3}	5	0.5	5×10^{-1}, 5×10^{-3}

(http://dx.doi.org/10.1016/j.flowmeasinst.2016.06.002)

In numerical simulations, as a performance evaluation index to evaluate the reconstruction performances for three methods, image error (IE) and correlation coefficient (CC) as defined earlier in equations (3.30) and (4.6) are used.

■ **Experimental setup**

The experimental data is obtained from the experimental setup developed by Jeju National University's research group with about 1% noise level (Kim *et al*. 2002b, Kim *et al.* 2002c).

The measurement system is composed of a cylindrical phantom with 32 electrodes, a data acquisition board with control software for voltage measurement, and current generator with switching board for current injection. Cylindrical phantom is filled with saline solution that has the resistivity of approximately 330 Ωcm up to the electrode's height of 20 cm . The plastic rods of diameter 1 cm and 2 cm with almost an infinite resistivity value are used as targets, and the currents with maximum amplitude 4.89 mA are injected through all the electrodes.

(a) Numerical results and discussion

Figure 4.10 shows the true and reconstructed images for numerical simulations. The true images for four cases are shown in the 1st row of figure 4.10. The reconstructed images obtained after 10 iterations using CRM, TV, l1-norm and PRM are shown from the 2nd row to 5th row in figure 4.10, respectively. All the images are shown with same color bar (300 to 2000 Ωcm). Figure 4.11 shows the two regions that are classified by Otsu's method after 1st iteration of Gauss-Newton algorithm with the conventional regularization method. The elements selected in figure 4.11 are considered as belonging to a sub-domain Ω_{BG} for each case.

In the 2nd row of figure 4.10, the reconstructed image using CRM has blurred boundaries of targets. In case 1, the target placed close to the center is not estimated well. In general, the reconstructed images using CRM have a low spatial resolution at the center region. This method makes the resistivity to be under-estimated, especially for cases 1, 2, and 4 which are placed near to the center. Also, the boundary of target is ambiguous. In the presence of noise, the reconstructed images using TV shown in the 3rd row of figure 4.10 have less spatial resolution, especially at the center region.

Multiple targets located close to each other near to the center have a poor reconstruction performance. However, for the targets located close to the boundary (case 3), the size and shape of the target are recovered. In the 4th row of figure 4.10, the reconstructed images using l1-norm have better spatial resolution compared to the CRM and TV. However, the target close to the center, especially with small size, is not reconstructed well like CRM and TV. In the 5th row of figure 4.10, the reconstructed images using PRM have better spatial resolution with distinct boundaries of the targets with improved estimation of resistivity distribution. Especially the background region has relatively uniform distribution compared to CRM and l1-norm. It is noticed that even if the targets are classified with irregular shape in figure 4.11, the reconstructed images using PRM show better spatial resolution.

Figure 4.12 shows the resistivity distribution about x-coordinate along the line on the true images in figure 4.10. As shown in the 2nd row of figure 4.10, in the case of CRM, the resistivity of targets is underestimated for all the four cases, and particularly the resistivity of the target located close to the center is more underestimated. The resistivity distribution estimated using TV has a uniform distribution in the target region while the resistivity values are underestimated in all the four cases. The resistivity distribution estimated using l1-norm is estimated well, relatively compared to the CRM and TV. However, the resistivity distribution of background between targets in case 2 and case 4 is still not estimated well. Also, the resistivity distribution of background has non-uniform distribution. However, the resistivity distribution estimated using PRM is shown closer to actual resistivity distribution compared to that using the other methods. Figure 4.13 shows the sorted resistivity distributions for each numerical case. The PRM curves have more flat region and steep slope compared to the other methods in all the cases. The results in figures 4.12 and 4.13 imply that PRM has uniform resistivity distribution in the background and more fast changes between the background and targets rather than the other methods.

The IE and CC results for all the numerical cases are shown in figures 4.14 and 4.15, respectively. As expected, the PRM has the better performance in the IE and CC results.

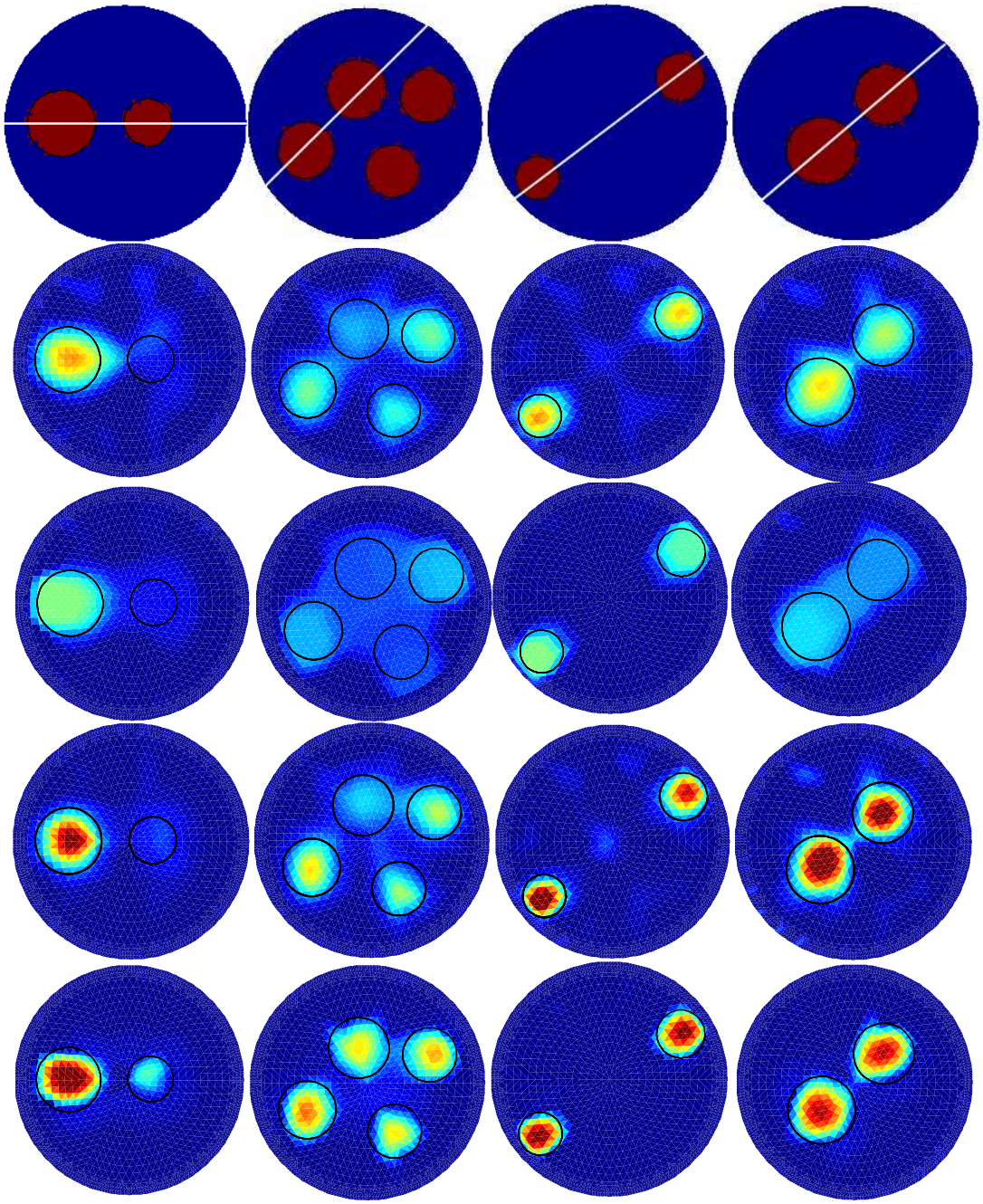

(a) (b) (c) (d)

Figure 4.10. Numerical results for two-phase flow monitoring with 1% noise: (a) case 1, (b) case 2, (c) case 3 and (d) case 4. True image and reconstructed images using CRM, TV, $l1$-norm, and PRM are given from the 1st row. The black circles in the image represent the true position of targets.

(http://dx.doi.org/10.1016/j.flowmeasinst.2016.06.002)

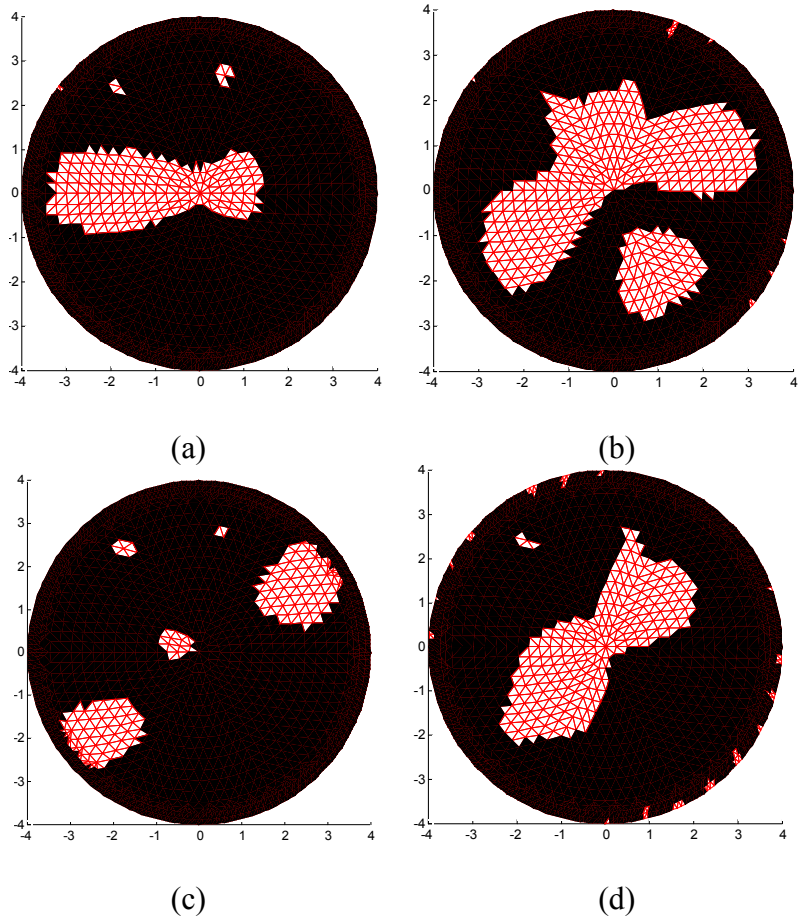

Figure 4.11. Two regions classified by Otsu's thresholding method after 1st iteration of Gauss-Newton algorithm for numerical cases: (a) case 1, (b) case 2, (c) case 3 and (d) case 4.

(http://dx.doi.org/10.1016/j.flowmeasinst.2016.06.002)

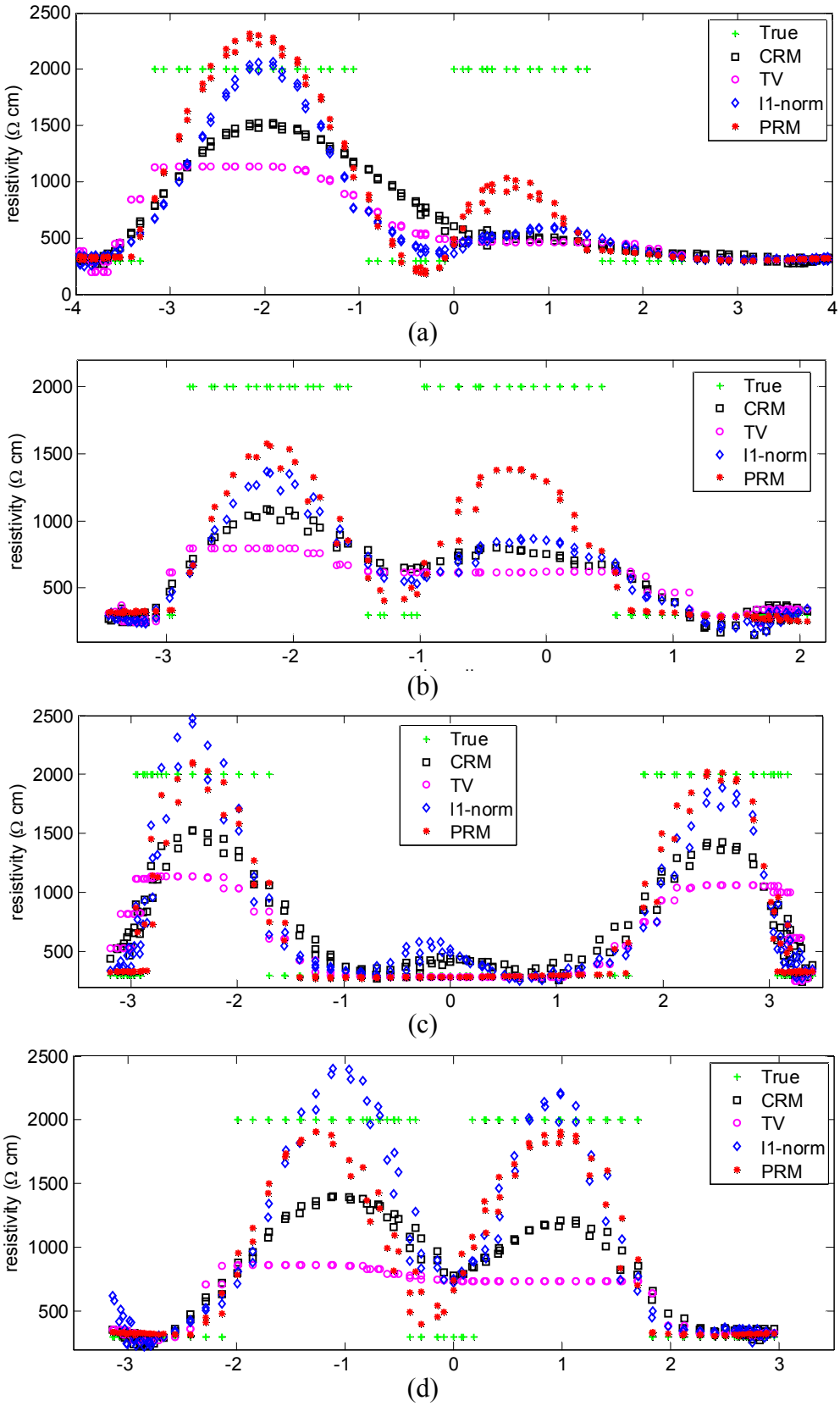

Figure 4.12. The resistivity distributions about x-coordinate along the line on the true images in figure 4.10 for numerical cases: (a) case 1, (b) case 2, (c) case 3 and (d) case 4

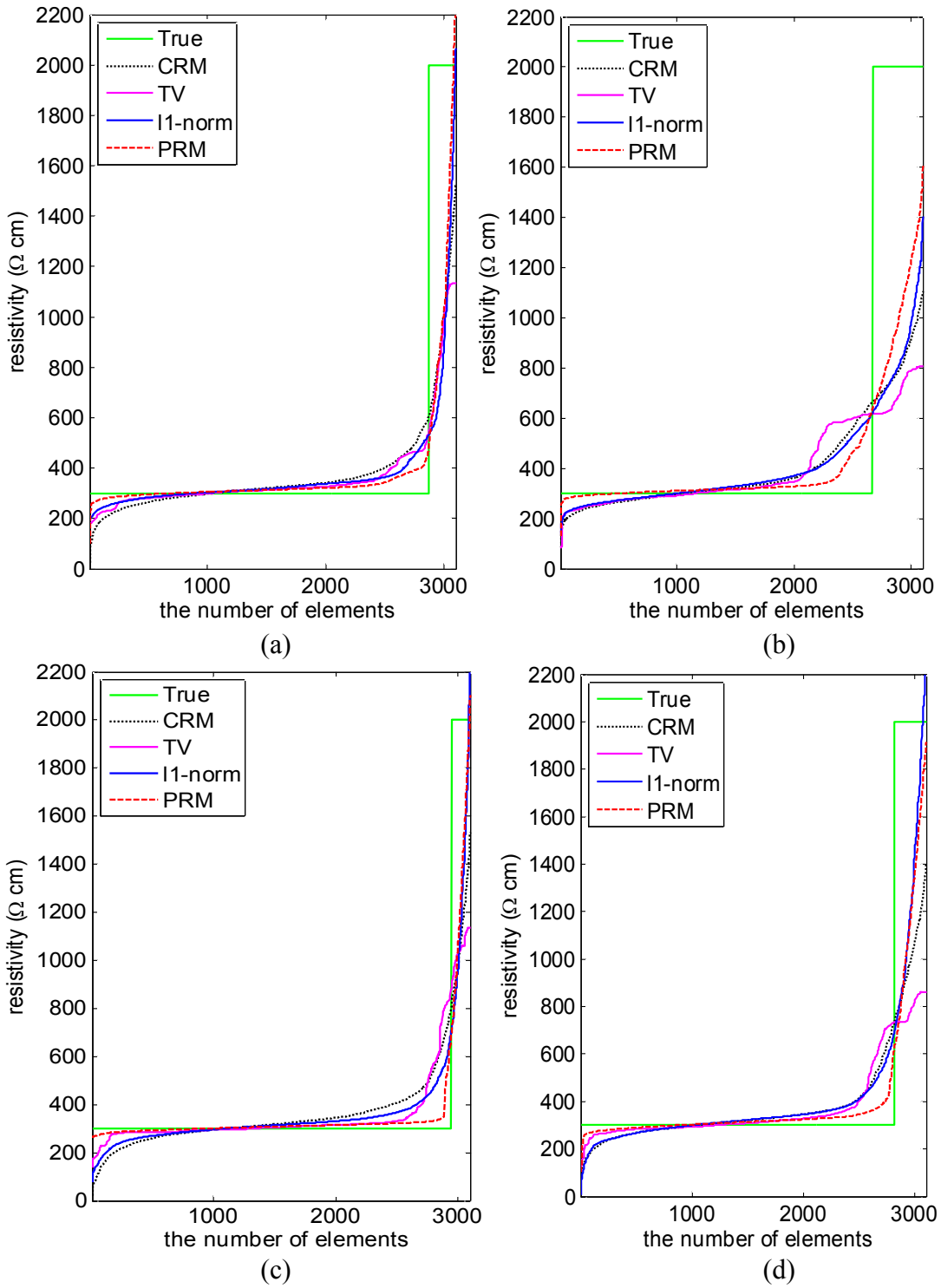

Figure 4.13. The sorted resistivity distributions for numerical cases: (a) case 1, (b) case 2, (c) case 3 and (d) case 4

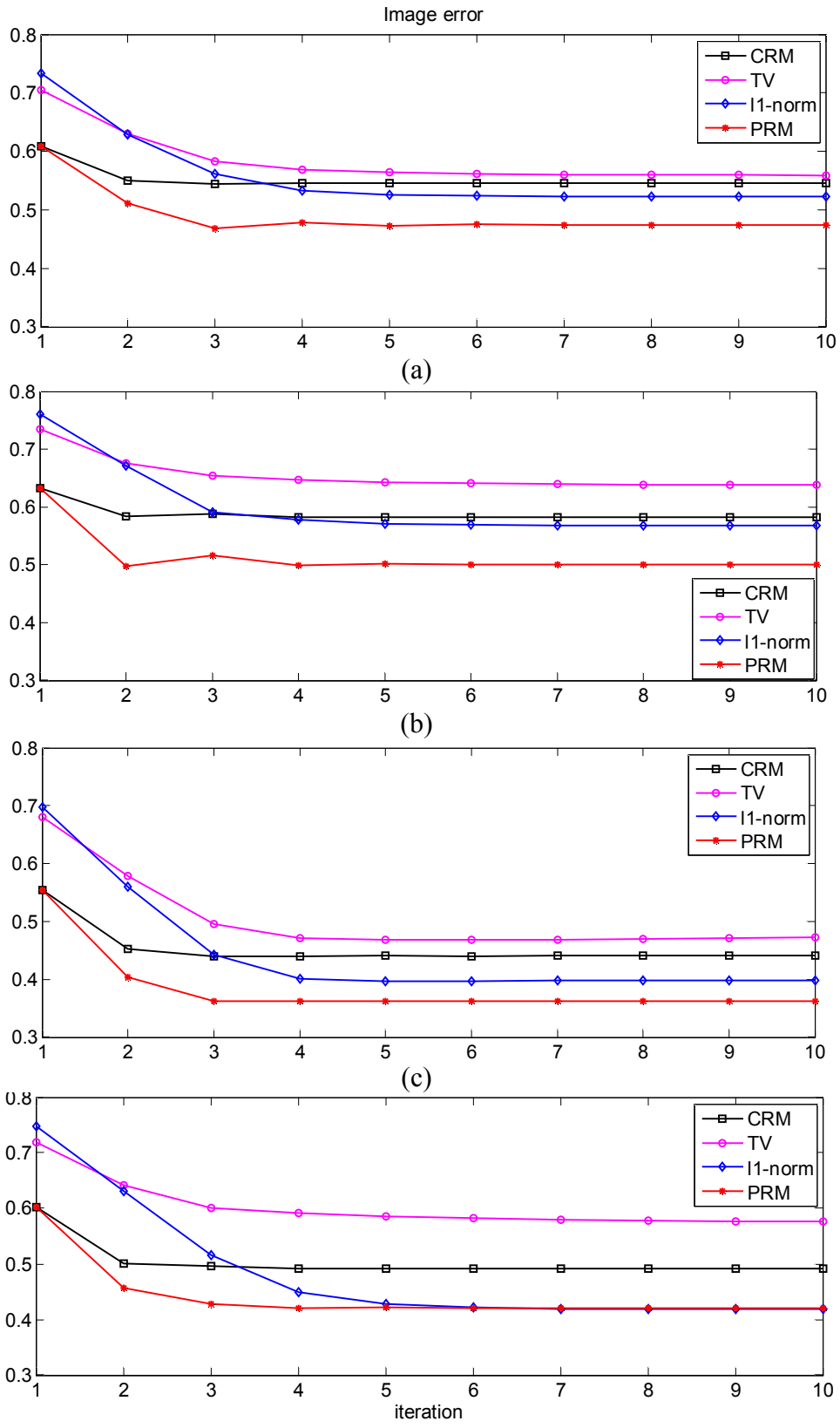

Figure 4.14. Image errors for numerical cases: (a) case 1, (b) case 2, (c) case 3 and (d) case 4

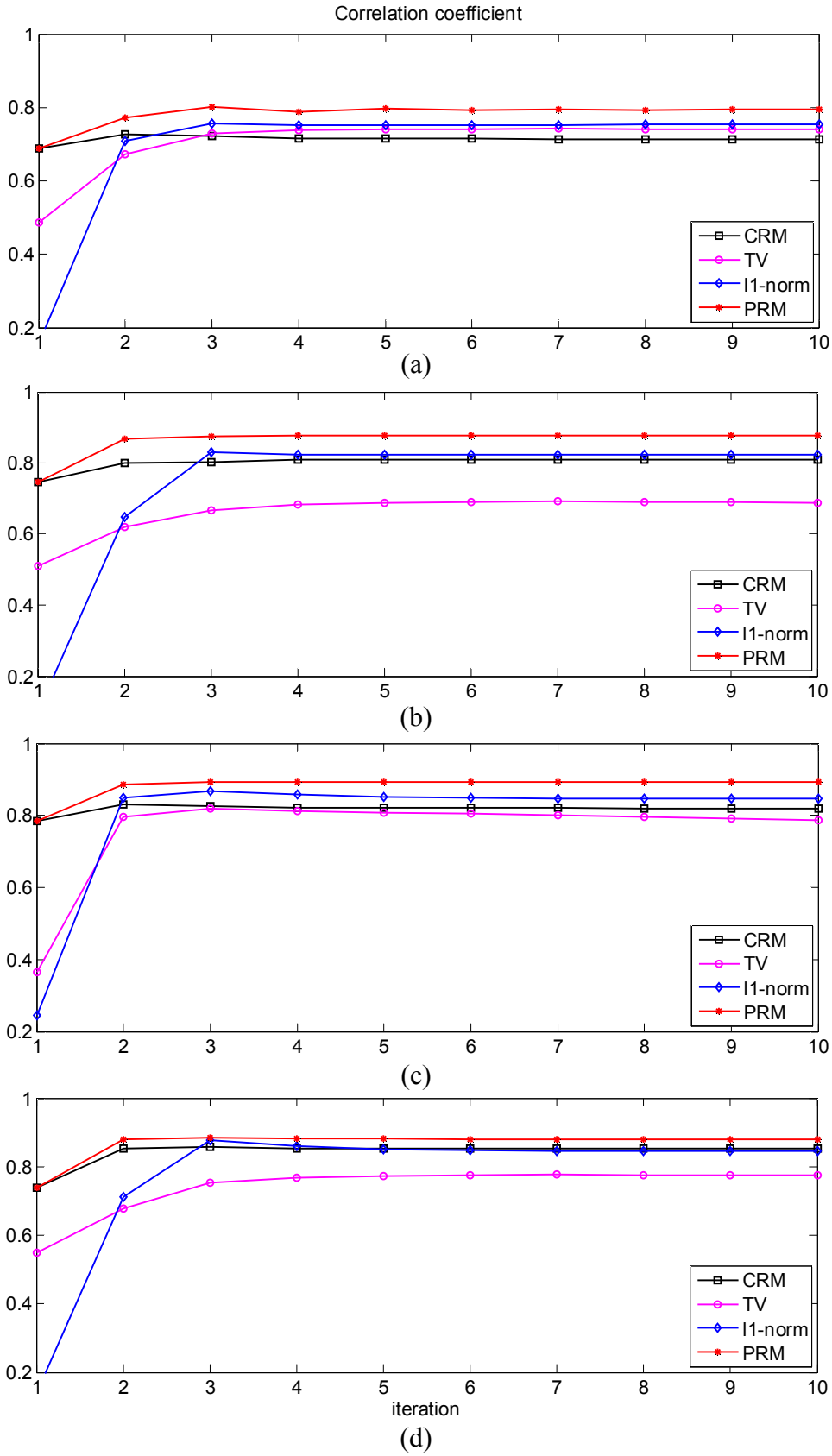

Figure 4.15. Correlation coefficients for numerical cases: (a) case 1, (b) case 2, (c) case 3 and (d) case 4

(b) Experimental results and discussion

The true images for four experimental cases are shown in the 1st row of figure 4.16, and the reconstructed images after 10 iterations using the Gauss-Newton algorithm with the CRM, TV, $l1$-norm and the PRM are shown from the 2nd row to 5th row in figure 4.16. Figure 4.17 shows two regions classified by Otsu's method after 1st iteration of Gauss-Newton algorithm with the conventional regularization method. All the reconstructed images in figure 4.16 are shown using same color bar (300 to 2000 Ωcm). The resistivity of targets by CRM and TV is underestimated compared to the $l1$-norm and PRM, especially, for the targets placed near to the center. In experimental case 1, the background regions using CRM, TV and $l1$-norm are not uniform with artifacts that can be misinterpreted as target. The reconstructed images by PRM have a better spatial resolution with the more uniform background and discrete boundary for target compared to the other methods.

Figure 4.18 shows the resistivity distribution about x-coordinate along the line in the 1st row of figure 4.16 for each experimental case. In figure 4.18, CRM and TV have an underestimated target resistivity compared to the $l1$-norm and PRM. The undesirable ripples in the background are shown in the resistivity distribution using CRM, TV and $l1$-norm compared to the PRM. Figure 4.19 shows the sorted resistivity distributions for each experimental case. In figure. 4.19, the PRM curves have more discrete transient on the boundary of targets and more uniform background similar to the numerical results. The results in figures 4.16 to 4.19 suggest that PRM has better reconstruction performance compared to the other methods.

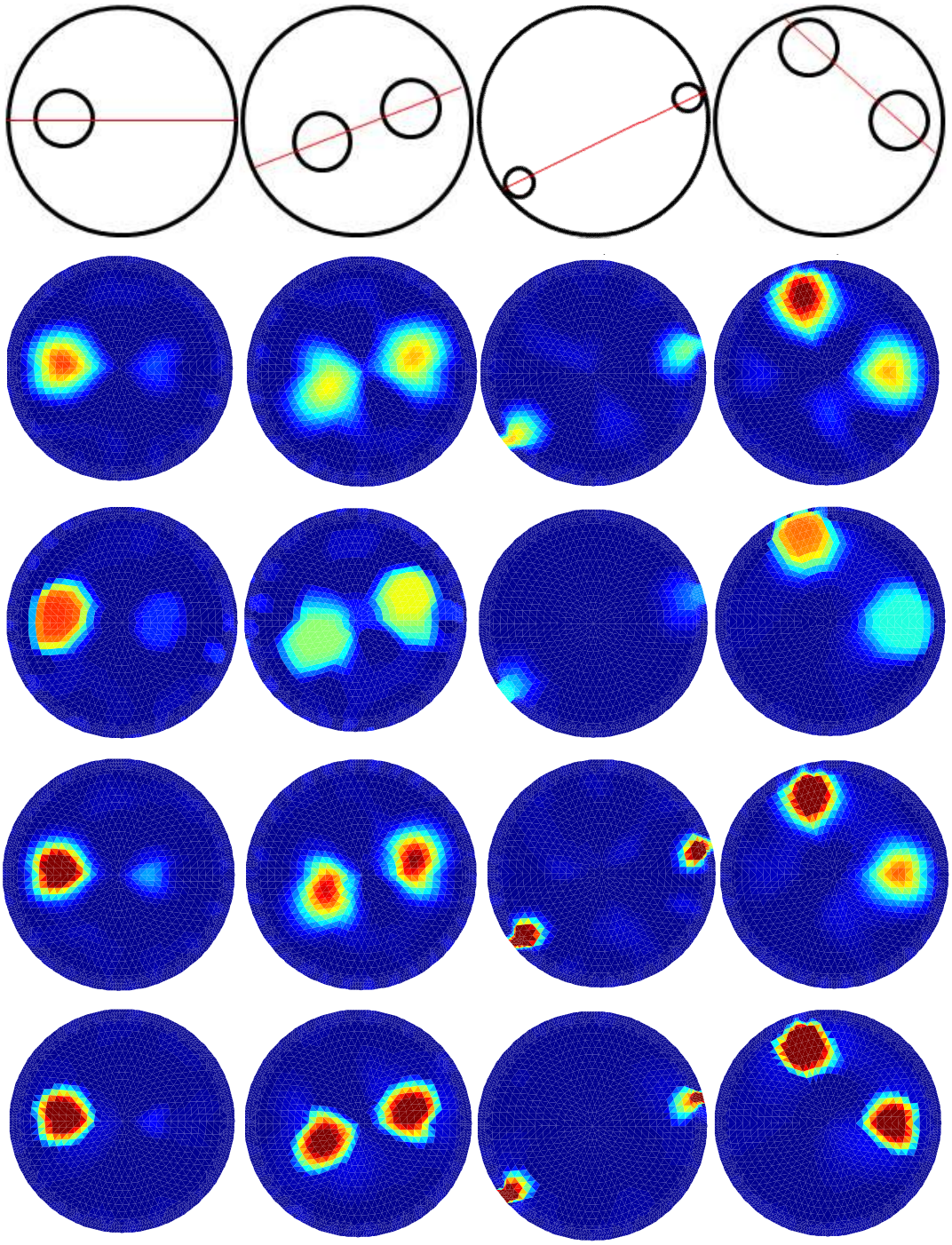

(a) (b) (c) (d)

Figure 4.16. Experimental results for two-phase flow monitoring: (a) case 1, (b) case 2, (c) case 3 and (d) case 4. True image and reconstructed images using CRM, *l*1-norm, TV and PRM are given from the 1st row.

(http://dx.doi.org/10.1016/j.flowmeasinst.2016.06.002)

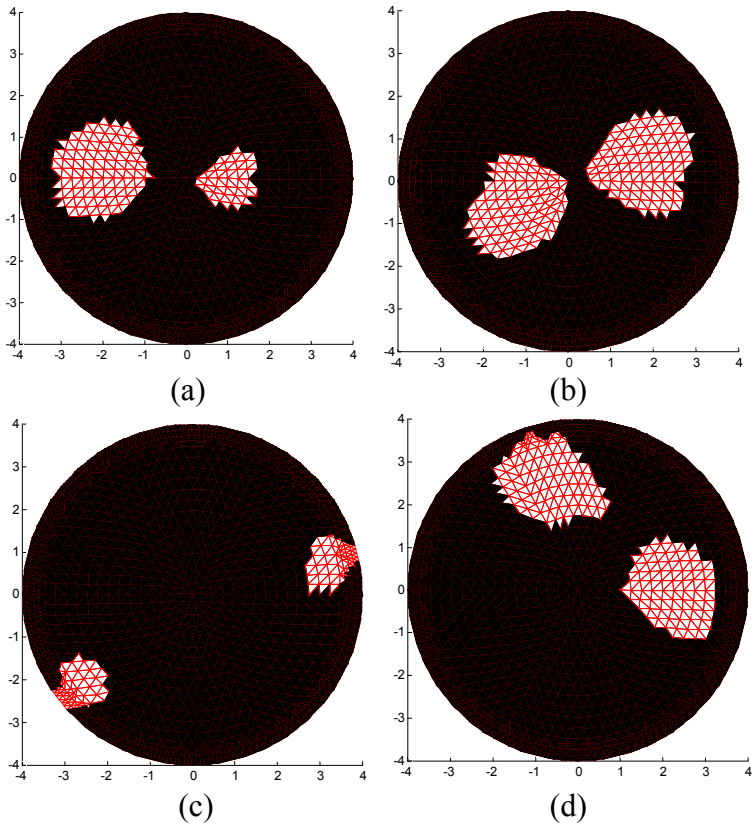

Figure 4.17. Two regions classified by Otsu's thresholding method after 1st iteration of Gauss-Newton algorithm for experimental cases: (a) case 1, (b) case 2, (c) case 3, and (d) case 4.

(http://dx.doi.org/10.1016/j.flowmeasinst.2016.06.002)

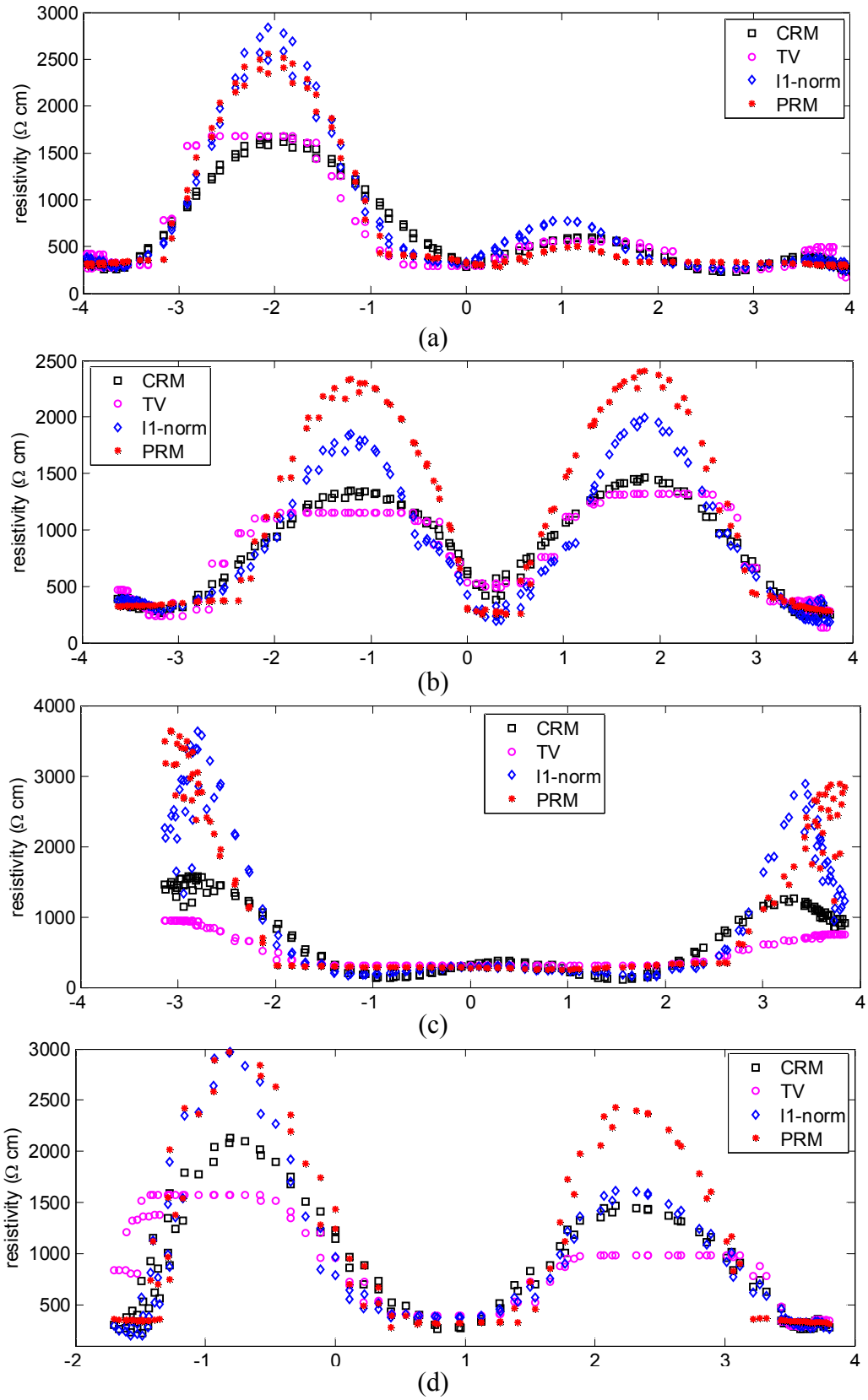

Figure 4.18. The resistivity distributions about x-coordinate along the line in the 1st row of figure 4.16 for experimental cases: (a) case 1, (b) case 2, (c) case 3, and (d) case 4

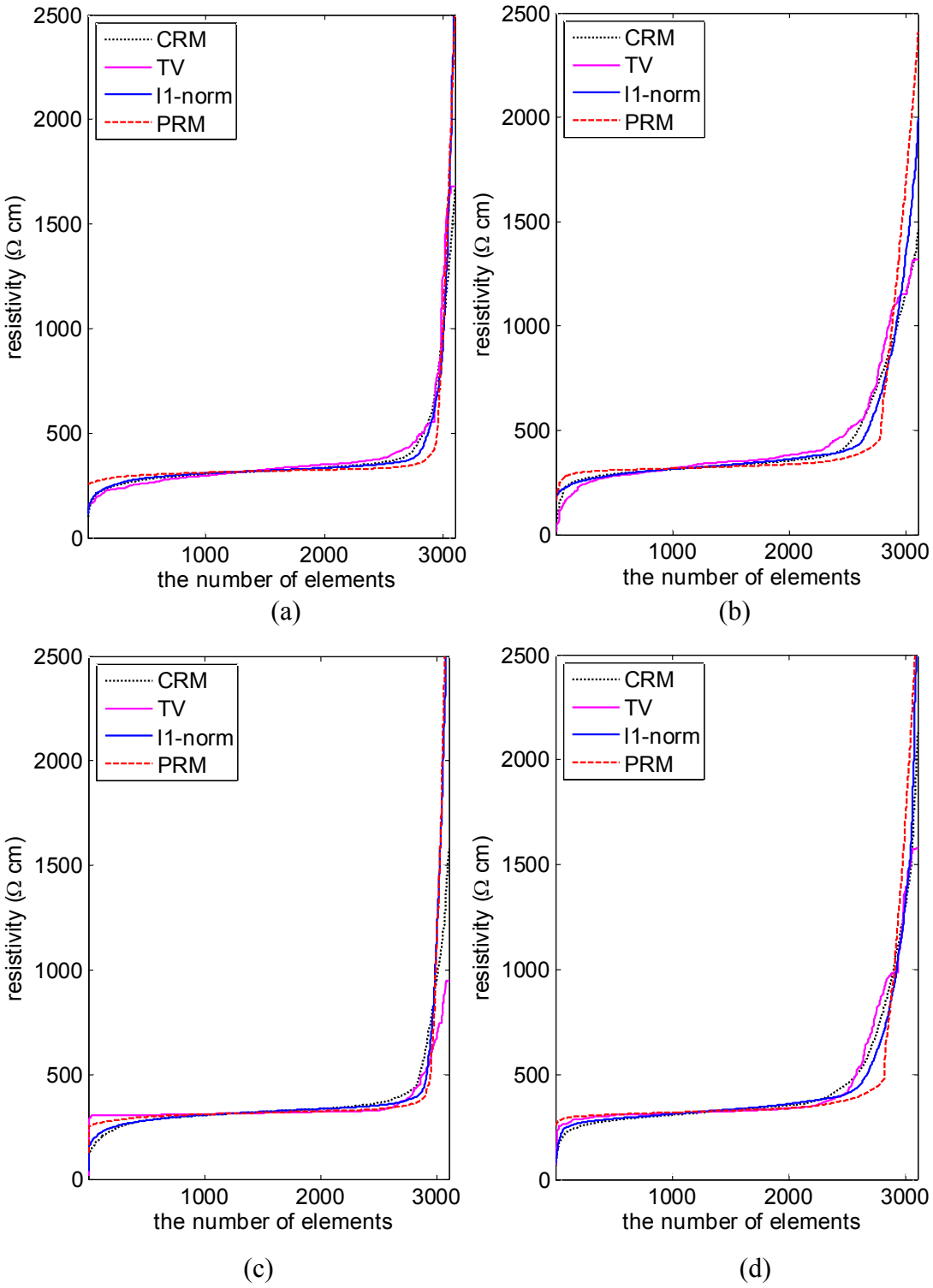

Figure 4.19. The sorted resistivity distributions for experimental cases: (a) case 1, (b) case 2, (c) case 3, and (d) case 4

5. Conclusions

Image reconstruction using electrical impedance tomography is highly ill-posed, therefore, the regularization method is required in the inversion process as an additional constraint from the *prior* information of the true solution. The reconstruction performance is heavily dependent on the type of regularization method. The generalized Tikhonov regularization using difference-type regularization matrix is used as a common regularization method in EIT. This conventional regularization method provides good stability of the inverse problem with rapid convergence, however, the image gets smoothen and it makes difficult to describe the sharp transition in boundary with different resistivity.

In order to have a desirable reconstructed image with better accuracy and by preserving sharp transition in boundary with different resistivities, a sub-domain based regularization method is proposed in this thesis. In the proposed regularization method, the partially known or guessed *prior* information of an internal structure is considered as a sub-domain. To impose the *prior* information into the proposed regularization method, the regularization matrix is anisotropically modified by considering sub-domains and the regularization parameter is assigned with different weights for the sub-domains. By doing so, the resistivity changes in the sub-domains have an effect on the resistivity changes within each sub-domain, however, the resistivity changes in the other regions except for the sub-domains are affected the resistivity changes in the whole domain. To investigate the performance of the proposed regularization method, two applications for human thorax monitoring and two-phase flow monitoring are considered.

In the human thorax monitoring, the situation with constant lung region and two different sizes' heart region during the cardiac cycle is considered. Also, CT image is considered as the *prior* information, and one-step Gauss-Newton algorithm is used for estimating internal resistivity distribution. Simulations with synthetic data and experimental data are computed with chest shape mesh. The sub-domain based regularization method has the improved spatial resolution with the more uniform resistivity distribution in the background and the more distinct boundaries of the lungs and heart.

In two-phase flow monitoring, the part of background is considered as a sub-domain. The sub-domain region is distinguished automatically using Otsu's thresholding method after 1st iteration of Gauss-Newton algorithm with the conventional regularization method. The reconstructed results with synthetic and experimental data are compared using iterative Gauss-Newton algorithm with the conventional regularization method and sub-domain based regularization method. Also, they are compared with the *l*1-norm and total variation regularization methods developed for non-smooth images. It can be noticed that the sub-domain based regularization method is successful in improving the spatial resolution of the reconstructed images with sharp boundary of targets and good accuracy compared to the other methods.

Further study will be carried out to test the three-dimensional reconstruction performance of the sub-domain based regularization method. In addition, the sub-domain concept will be extended with other regularization methods such as the total variation and *l*1-norm regularization methods.

Summary

Electrical impedance tomography (EIT) is a non-invasive imaging technique in which the internal resistivity distribution is reconstructed based on the injected currents and measured voltages on the electrodes which are attached to the boundary of an object.

The image reconstruction in EIT is usually treated as least squares problems, and Gauss-Newton algorithm is widely used to estimate the resistivity because of its rapid convergence and an estimated accuracy. However, since EIT has highly ill-posed inverse problem, the regularization method is used to mitigate the ill-posed nature and reconstruct the meaningful image. The regularization method plays an important role in the spatial resolution in EIT. The generalized Tikhonov regularization method using difference-type regularization matrix is commonly used because of the most convenient in computational time and convergence stability of the inverse problem. However, this method is impossible to recover the discrete resistivity distribution in the image reconstruction due to its smoothness assumption.

To improve the spatial resolution by overcoming this problem, a sub-domain based regularization method is used when the partial information on the internal structure is known or available. In the sub-domain based regularization method, a part of whole domain is considered as a sub-domain, such prior information is incorporated into the regularization method. In order to do so, the regularization matrix is anisotropically modified to contain prior information on a sub-domain and the regularization parameter is set with different weight for the sub-domain. With this, the resistivity changes in the sub-domain have an effect on the resistivity changes within the sub-domain, however, the resistivity changes outside the sub-domain are affected the resistivity changes in the whole domain.

To illustrate the reconstruction performance of the sub-domain based regularization method, two applications, i.e., human thorax monitoring and two-phase flow monitoring, are considered. The results of computer simulations for synthetic and experimental data show that the sub-domain based regularization method has the improved reconstruction performance than the conventional method.

References

Adler A and Guardo R 1996 Electrical impedance tomography: regularized imaging and contrast detection *IEEE Trans. Med. Imaging* **15** 170-179

Barber D C and Brown B H 1984 Applied Potential tomography *J phys. E: Sci Instrum* **17** 723-733

Baysal U and Eyuboglu B M 2000 Tissue resistivity estimation in the presence of positional and geometrical uncertainties *Physics in Medicine and Biology* **45**(8) 2373-2388

Borsic A, Lionheart W R B and McLeod C N 2002 Generation of Anisotropic-Smoothness Regularization Filters for EIT detection *IEEE Trans. Med. Imaging* **21** 579-587

Borsic A, Graham B M, Adler A and Lionheart W R B 2007 Total Variation Regularization in Electrical Impedance Tomography *MANCHESTER* **1824** 1-26

Brenner S C and Scott L R 1994 *The Mathematical Theory of Finite element Method*, Springer

Brown B H 2001 Medical impedance tomography and process impedance tomography: a brief review *Meas. Sci.Technol.* **12** 991–6

Bruder H, Scholz B and Abrahamfuchs K 1994 The influence of inhomogeneous volume conductor models on the ECG and the MCG *Physics in Medicine and Biology* **39**(11) 1949-68

Cartwright D J 2001 *Underlying Principles of the Boundary Element Method* WIT

Casas A, Himi M, Diaz Y, Pinto V, Font X and Tapias J C 2008 Assessing aquifer vulnerability to pollutants by electrical resistivity tomography (ERT) at a nitrate vulnerable zone in NE Spain *Environ. Geol.* **54** 515-520

Cheney M, Isaacson D, Newell J C, Simske S and Goble J. 1990 NOSER: An algorithm for solving the inverse conductivity problem *Int. J. Imaging Syst. Technol.* **2** 66-75

Cheney M and Isaacson D 1992 Distinguishability in impedance imaging *IEEE Trans. Biomed. Eng.* **39** 852-860

Cheney M, Isaacson D and Newell J C 1999 Electrical impedance tomography *SIAM Review* **41** 85-101

Cheng K S, Isaacson D, Newell J C and Gisser D G 1988 Error comparison for different current patterns in electrical impedance tomography *in proc 10 th Intl Conf IEEE Eng Med Biol Society* **37** 60-65

Cheng K S, Isaacson D, Newell J C and Gisser D G 1989 Electrode models for electric current computed tomography *IEEE Trans. Biomed. Eng.* **36** 918-924

Cherepenin V A, Karpov A Y, Korjenevsky A V, Kornienko V N, Kultiasov Y S, Ochapkin M B, Trochanova O V, and Meister J D 2002 Three-dimensional EIT imaging of breast tissues: System design and clinical testing *IEEE Trans. Med. Imag.* **21** 662–667

Choi M H, Kao T J, Isaacson D, Saulnier G J and Newell J C 2004 A simplified model of mammography geometry for breast cancer imaging with electrical impedance tomography *in Proc. 26th Annu. Int. Conf. IEEE EMBS, San Francisco* 1310-1313

Chung E T, Chan T F and Tai X C 2005 Electrical impedance tomography using level set representation and total variational regularization *J. Comput. Phys.* **205** 357–372

de Munck J C, Faes T J C and Heethaar R M 2000 The Boundary Element Method in the Forward and Inverse Problem of Electrical Impedance Tomography *IEEE Trans. Biomed. Eng.* **47** 792-800

Dai T 2008 Image Reconstruction in EIT Using Advanced Regularization Frameworks *Carleton University, Canada, Doctoral Dissertation*

Dai T and Adler A 2008 Electrical impedance tomography reconstruction using *l*1 norms for data and image terms *30th Annual International IEEE EMBS Conference, Vancouver, British Columbia, Canada,* 2721-2724

Daily W, Ramirez A 1992 Electrical resistivity tomography of vadose water movement *water resource research* **28** 1429-1442

Dickin F and Wang M 1996 Electrical resistance tomography for process tomography *Meas.Sci.Technol.* **7** 247-260

Dobson D C, Santosa F 1994 An Image enhancement technique for electrical impedance tomography *Inverse Problems* **10**(2) 317-334

Fuhry M and Reichel L 2012 A new Tikhonov regularization method *Numerical Algorithms* **59**(3) 433-445

Gehre M, Kluth T, Lipponen A, Jin B, Seppanen A, Kaipio J P and Maass P 2012 Sparsity reconstruction in electrical impedance tomography: An experimental evaluation *Journal of Computational and Applied Mathematics* **236** 2126-36

George D L, Torczynski J R, Shollenberger K A, O'Hern T J and Ceccio S L 2000 Validation of electrical-impedance tomography for measurements of material distribution in two-phase flows *International Journal Multiphase Flow* **26** 549-581

Gisser D C, Isaacson D and Newell J C 1988 Theory and performance of adaptive current tomography system *Clinical Physics and Physiological Meas.* **9** 35-42

Golub G H, Heath M and Wahba G Generalized cross-validation as a method to choosing a good ridge parameter *Technometrics* **21**(2) 215-223

Hanke M 1996 Limitations of the L-curve method in ill-posed problems, *BIT* **36** 287-301

Hansen P C 1992 Analysis of discrete ill-posed problems by means of the L-curve, *SIAM Rev*. **34** 561-580

Hansen P C 1994 Regularization Tools: A Matlab Package for Analysis and Solution of Discrete Ill-Posed Problems *Numerical algorithms* **6**(1) 1-35

Heikkinen L M, Vauhkonen M, Savolainen T, Leinonen K and Kaipio J P 2001 Electrical process tomography with known internal structures and resistivities *Inverse Problems in Engineering* **9** 431-54

Holder D S 1992 Electrical impedance tomography (EIT) of brain function *Brain Topogr.* **5** 87–93

Holder D S 2005 *Electrical Impedance Tomography: Methods, History and Application* IOP Publishing Ltd

Hua P, Webster J G and Tompkins W J 1988 A regularised electrical impedance tomography reconstruction algorithm *Clin. Phys. Physiol. Meas.* **9** 137-41

Isaacson D 1986 Distinguishability of conductivities by electric current computed tomography *IEEE Trans. Med. Imag.* **M1-5** 91-95

Isaacson D and Cheney M 1990 Current problems in impedance imaging *Inverse problems in partial differential equations* 141-149

Jain H, Isaacson D, Edic P M and Newell J C 1997 Electrical impedance tomography of complex conductivity distributions with noncircular boundary *IEEE Trans. Biomed. Eng.* **44** 1051-1060

Jin B, Khan T and Maass P 2011 A reconstruction algorithm for electrical impedance tomography based on sparsity regularization *Int. J. Numer. Methods Eng*. **89** 337-353

Jones O C, Lin J T, Ovacik L and Shu H 1993 Impedance imaging relative to gas-liquid systems *Nuclear Engineering and Design* **141** 159-176

Kaipio J P, Kolehmainen V, Vauhkonen M and Somersalo E 1999 Construction of nonstandard smoothness priors *Inverse Problems* **15** 713-729

Kang S I, Khambampati A K, Jeon M H, Kim B S and Kim K Y 2016a A sub-domain based regularization method with prior information for human thorax imaging using electrical impedance tomography *Meas. Sci. Technol.* **27**(2) 25703-25711

Kang S I, Khambampati A K, Kim B S and Kim K Y 2016b EIT image reconstruction for two-phase flow monitoring using a sub-domain based regularization method *Flow Measurement and Instrumentation* (in press)

Kang S I and Kim K Y 2016 Performance comparision of regularization methods in electrical resistance tomography *Journal of IKEEE* **20**(3) 226-234

Kerner T E, Paulsen K D, Hartov A, Soho S K and Poplack S P 2002 Electrical impedance spectroscopy of the breast: clinical results in 26 subjects *IEEE Trans. Med. Imag.* **21** 638–645

Khambampati A K, Lee B A, Kim K Y and Kim S 2012 An analytical boundary element integral approach to track the boundary of a moving cavity using electrical impedance tomography *Meas. Sci. Technol.* **23**(035401) 1-17

Kim M C, Kim S, Kim K Y and Lee Y J 2001 Regularization methods in electrical impedance tomography technique for the two-phase flow visualization *International Communications in Heat and Mass Transfer* **28** 773-782.

Kim K Y, Kang S I, Kim M C, Kim S, Lee Y J and Vauhkonen M 2002a Dynamic Image Reconstruction in Electrical impedance Tomography with Known Internal Structures *IEEE Trans. Mag.* **38**(2) 1301-1304.

Kim M C, Kim S, Lee H J, Kim K Y and Anghaie S 2002b An experimental study of electrical impedance tomography for the two-phase flow visualization *Int. Commun.Heat Mass Trans.* **29** 193-202

Kim M C, Kim K Y, Kim S, Lee H J and Lee Y J 2002c Electrical Impedance tomography for the visualization of the phase distribution in an annular tube. *Journal of Industrial and Engineering Chemistry* **8**(2): 168-172.

Kim B S, Boverman G, Newell J C, Saulnier G J and Isaacson D 2007 The complete electrode model for EIT in mammography geometry *Physiol. Meas.*28 S57-S69

Maillol J M, Seguin M K, Gupta O P, Akhauri H M and Sen N 1999 Electrical resistivity tomography survey for delineating uncharted mine galleries in West Bengal, India. *Geophys. Prospect., Eur. Assoc. Geosci. Eng.* 47 103–116.

Mamatjan Y, Borsic A, Gursoy D and Adler A 2012 Electrical Impedance Tomogrpahy Image Reconstruction with *l*1 data and image norms *Journal of IEEE TBME* 1-11

Mueller J L, Isaacson D and Newell J C 1999 A reconstruction algorithm for electrical impedance tomography data collected on rectangular electrode arrays *IEEE Trans. on Biomed. Eng.* **46** 1379-86

Mueller J L, Isaacson D and Newell J C 2001 Reconstruction of conductivity changes due to ventilation and perfusion from EIT data collected on a rectangular electrode array *Physiol. Meas.* **22** 97–106

Osterman K S, Kerner T E, Williams D B, Hartov A, Poplack S P and Paulsen K D 2000 Multifrequency electrical impedance imaging: preliminary in vivo experience in breast *Physiol. Meas.* **21** 99–109

Otsu N 1979 A threshold selection method from gray-level histograms *IEEE Transactions on Systems, Man, and Cybernetics* **SMC-9** 62-66.

Pinheiro P A T, Loh W W and Dickin F J 1997 Smoothness-constrained inversion for two-dimensional electrical resistance tomography *Meas. Sci.Technol*. **8** 293-302

Polydorides N and Lionheart WRB 2002 A MATLAB toolkit for three-dimensional electrical impedance tomography: A contribution to the electrical impedance and diffuse optical reconstruction software project, *Meas. Sci. Technol.* **13** 1871-1883

Rashid A, Kim B S, Khambampati A K, Kim S and Kim K Y 2011 An oppositional biogeography-based optimization technique to reconstruct organ boundaries in the human thorax using electrical impedance tomography *Physiol. Meas.* **32** 767-796

Reynolds J M and Taylor D I 1996 Use of geophysical surveys during the planning, construction and remediation of landfills *Geological Society, London, Engineering Geology Publications* **11** 93-98

Somersalo E, Cheney M and Isaacson D 1992 Exsistence and uniqueness for electrode models for electirc current computed tomography *SIAM J. Appl. Math.* **52**(4) 1023-1040

Vauhkonen M 1997 Electrical Impedance Tomography and Prior Information *Dept. of Applied Physics, University Kuopio, Doctoral Dissertation.*

Vauhkonen M, Vadasz D, Karjalainen P A, Somersalo E and Kaipio J P 1998 Tikhonov Regularization and Prior Information in Electrical Impedance Tomography *IEEE Trans. On Medical Imaging* **17**(2) 285-93

Webster J G 1990 Electrical Impedance Tomography *IOP Publishing Ltd.*

Williams R A and Beck M S 1995 *Process Tomogrpahy: Principles, Techniques and Applications* Butterworth-Heinemann, Oxford

Yang Y, Jia J, Polydorides N, and McCann, H 2014 Effect of structured packing on EIT image reconstruction *In Imaging Systems and Techniques (IST), 2014 IEEE International Conference on IEEE* 53-58

Yang W Q and Peng L 2003 Image reconstruction algorithms for electrical capacitance tomography *Mea. Sci. Technol.* **14** 1-13.

Yorkey T J and Webster J G 1987 A comparison of impedance tomographic reconstruction algorithms *Clin. Phys. Physiol. Meas.* **8(***Supplement A***)** 55-62

Yorkey T J, Webster J G and Tompkins W J 1987 Comparing reconstruction algorithms for electrical impedance tomography *IEEE Trans. Biomed. Eng*. **34** 843-853

감사의 글

어려움 많은 박사과정이었지만, 매 순간 작은 일에 최선을 다하면 결국 세상을 변하게 할 수 있다라는 중용 23 절의 구절을 되새기면서 나를 변화시키고자 길고도 짧은 4 년 반 동안의 기간을 보낸 것 같습니다. 그래서인지 보잘 것 없지만 작은 결실을 맺고 보니 너무 뿌듯하고 기쁩니다. 논문을 완성할 수 있도록 도움을 주신 분들께 감사의 말씀을 전하며 이 논문을 마무리하고자 합니다.

우선, 부족한 저를 신경써 주시고 채찍질 해주신 지도 교수님인 김경연 교수님께 무엇보다 감사드립니다. 그리고 바쁜신 가운데도 논문 심사를 하러 먼길 와 주신 이인수 교수님께도 감사드립니다. 또한 전자공학전공의 세 분의 논문 심사위원인 고성택교수님, 강민제교수님 및 고석준교수님을 비롯한 전자공학전공 김경식교수님, 이광만교수님, 도양회 교수님께도 감사드립니다.

박사과정 동안 한 연구실에서 많은 조언과 힘이 되 준 김봉석 박사님, 아닐 박사님, 그리고 석사 졸업생 현종호와 전민호, 박사과정 스라반쿠마르에게 감사의 마음을 전합니다. 그리고 전자공학전공 고경필 조교, 좌아름 조교님께도 감사의 마음을 전합니다. 이 분들의 앞날에 무궁한 발전이 있으시길 바랍니다.

오랜 기간 배려해주고 응원해 준 친정식구와 시댁식구 모두에게 고맙고 감사드립니다. 마지막으로, 매 순간마다 든든한 버팀목이 되어 준 나의 남편과 세 딸 유림, 유진, 유은에게 감사의 말 전합니다.

사랑하는 나의 가족과 존재만으로도 고마운 아버지께 논문을 받칩니다.